Part I

Low-Order Model of Martian Circulation

Chapter 1 Introduction

The objective of this thesis is the construction of a low-order model of the martian global circulation suitable for conducting long-term (decadal) studies of the martian climate and application of this model to the problem of interannual variability of the GDSs. The idea is to construct a computationally fast model by retaining only the main elements of the global circulation (i.e., Hadley cell). The speed and simplicity of the LOM allows one to perform long-term simulations of the variability of the martian atmospheric system, - a prohibitive task with more sophisticated GCMs.

Simplified models of the martian global circulation have been published. They include the zonally symmetric models [HLP82, MHTP93] and truncated spectral models [HHBY97, MI80]. In the zonally symmetric models longitudinal variations are neglected, while in the spectral models the set of basis functions is severely truncated to yield the state space of lesser dimension. These models were used to simulate GDSs and water transport in the martian atmosphere. However, no attempts to study interannual variability were made.

LOMs are the simplest models. They usually consist of just a few independent variables. The LOMs are widely used in studies of Earth's climate [TSCJ94, Fra78, SM80, Has76], the most famous example being the Lorenz system [Lor63]. Lately, LOMs were successful in modeling the El Niño-Southern Oscillation phenomenon [TSCJ94]. This work is the first attempt to simulate interannual variability on Mars with a LOM.

The LOM is constructed by Galerkin projection of a 2D (longitudinally averaged) GCM onto a truncated set of basis functions. The model describes the Hadley part of the general circulation. The effects of waves and eddies are parameterized as Rayleigh friction. Thermal forcing is included in the Newtonian cooling term. Strength of the surface dust source depends on the strength of the atmospheric winds, allowing dust storms to develop naturally.

Part I of the thesis presents the description of the model and discusses its results. Chapter 2 describes the method by which the model was constructed. It also outlines the simplified way by which the atmosphere and surface are coupled. The model's performance for clear and dusty conditions is compared to the NASA Ames GCM [PHSL90] and it is found that the simulated mean meridional circulation and temperature fields compare reasonably well. The date of occurrence and duration of the global dust storms produced by the model also compare well with observations by VLs. In Chapter 3 it is shown that the LOM without dust can be approximated as the Lorenz system with forcing. This circumstance allows one to define the boundaries of different regimes in the behavior of the LOM. Chapter 4 summarizes Part I of the thesis. In Part II of the thesis the model is used to simulate the interannual variability of GDSs. Chapter 5 offers a brief introduction to the subject. In Chapter 6 the behavior of the model with deterministic forcing is examined and it is found that for realistic parameter values the model does not produce interannual variability. In Chapter 7 a stochastic component is added to the forcing of the model. It is shown that in this configuration the model is capable of producing interannual variability. The results are very dependent on the degree of coupling between atmosphere and surface. Chapter 8 summarizes results of the model simulations and discusses the implications of the results for martian climate studies.

Chapter 2 Model Description

2.1 Model Domain

The model is a longitudinally averaged 2D model. The model domain extends vertically from the surface ($z = 0$ km, $p = p_s$) to the top of the atmosphere ($z \sim 50$ km, $p = p_t$), where z is height, p is pressure, p_s is surface pressure and p_t is pressure at the top of the atmosphere. The pressure at the top of the atmosphere p_t was fixed at 0.07 mbar, while p_s changes seasonally, reaching its maximum of ~ 7 mbar at perihelion. The model extends horizontally from $\theta = -45°$ to $\theta = 45°$, where θ is latitude. The vertical extent of the model approximately corresponds to the vertical extent of the Ames GCM [PHSL90], while the horizontal extent corresponds to the maximum extent of the Hadley cell in the GCM simulations. The model is only applicable to the Hadley part of the global circulation. There is no interaction with the polar regions. The choice of the model domain is dictated by simplicity considerations, since inclusion of the polar regions would require a more complex set of basis functions to describe the dynamics of the atmospheric flows. On the other hand, interaction between polar and mid-latitude-equatorial regions is only important during spring and fall, when the polar caps are subliming and condensing [PHSL90, HPB$^+$93].

2.2 Atmospheric Component

2.2.1 Primitive equations

The dynamics of the axially symmetric atmospheric motion is described by the zonally averaged primitive equations in spherical coordinates:

$$\frac{\partial u}{\partial t} = -v\frac{\partial u}{\partial y} - \omega\frac{\partial u}{\partial p} + v\left(f + \frac{u\tan\theta}{r_m}\right) - ru \tag{2.1}$$

$$\frac{\partial v}{\partial t} = -v\frac{\partial v}{\partial y} - \omega\frac{\partial u}{\partial p} - u\left(f + \frac{u\tan\theta}{r_m}\right) - \frac{\partial \Phi}{\partial y} - rv \tag{2.2}$$

$$\frac{\partial T}{\partial t} = -v\frac{\partial T}{\partial y} - \omega\frac{\partial T}{\partial p} + \frac{\kappa T\omega}{p} + Q \tag{2.3}$$

$$\frac{\partial \Phi}{\partial p} = -\frac{RT}{p} \tag{2.4}$$

$$\frac{\partial p_s}{\partial t} = -\frac{\partial \omega}{\partial p} - \frac{\partial(\cos\theta v)}{\cos\theta \partial y} \approx 0 \tag{2.5}$$

The above equations are the zonal and meridional momentum equations, the thermodynamic energy equation, the hydrostatic equation, and the mass continuity equation, respectively. The system of equations (2.1)-(2.5) is written for the Eulerian mean circulation [Hol92] rather than for the residual mean circulation for the purpose of comparing results with the GCM [PHSL90]. The terms $-ru$ and $-rv$ in Eqs. (2.1)-(2.2), where r is a Rayleigh friction coefficient, can be regarded as a parameterization of eddy flux divergences. The value of r is discussed in Section 2.8.

The independent variables are the horizontal coordinate y (positive northward), pressure p, and time t. The prognostic dependent variables are the zonal component of horizontal velocity (positive eastward) u, the meridional component (positive northward) v, and the temperature T. The geopotential Φ and pressure velocity $\omega = dp/dt$ are diagnostic dependent variables. Finally, $f = 2\Omega\sin\theta$ is the Coriolis parameter, Ω is the planetary rotation rate, θ is latitude, r_m is planetary radius ($y = r_m\theta$), p_s is the surface pressure, R is the gas constant, $\kappa = R/C_p$, and C_p is the specific heat at constant pressure.

The 2D approximation is adequate for representation of the Hadley circulation on Mars. 2D models neglect longitudinal features such as transient and stationary planetary waves and eddies. However, the 3D GCM simulations ([HPB$^+$93, PHSL90]) indicate that the kinetic energy ([HPB$^+$93], Fig. 1) and heat fluxes ([PHSL90], Fig. 6) associated with eddies are much smaller than the energy and heat flux associated with the Hadley cell. Comparison of the 2D and 3D GCM simulations of the GDS ([MPH$^+$95, MHTP93]) show that in the 2D case dust remains confined to the region between 40°N and 50°S, while in the 3D case dust extends over the south polar cap

and into the northern polar regions ([MPH+95], Fig. 4). The difference is due to the action of transient and standing eddies. As a result, the dust optical depth in the SH in the 2D case is larger by a factor of about 2 during the active (sols 0 to 10) and decaying (sols 10 to 50) phases of the GDS. However, the difference in the strength of the meridional winds is smaller (of the order of 10%), since for the levels of atmospheric dustiness during the GDS (optical depth 10 in SH and 5 in NH at sol 10, and optical depth 4 in SH and 2 in NH at sol 25) the effect of dust on meridional circulation levels off ([MPH+95], Fig. 7).

The change of atmospheric mass due to sublimation and condensation of CO_2 was assumed to be slow enough so that $\partial p_s/\partial t$ in Eq. (2.5) can be neglected. However, the change of atmospheric mass was accounted for by including the seasonal surface pressure cycle derived from Viking observations [HFT95]. This neglects feedback between atmospheric temperature and surface pressure, but deviations of pressure from the seasonal mean [HFT95] are small - of the order of 10% even during a GDS [Til85, HRT+80]. Condensation mass flow was also neglected, but GCM simulations indicate that it "...has very little effect on simulated zonal-mean zonal winds ..." ([HPB+93]). The GCM simulations in which the condensation flow was set to zero show that "...the condensation flow mainly determines the strength of polar cap surface winds ..." ([HPB+93], Fig. 42).

Topography was neglected and no pressure gradient at the ground was assumed, so that $\partial p_s/\partial y = 0$. The GCM simulations with flat topography ([HPB+93], Fig. 43) show that the surface winds and mean meridional circulation are stronger in the simulations without topography, due to decreased frictional interaction with the surface. However, "...the main effect of topography on mean circulation is confined to lower levels ..." ([HPB+93]). Indeed, Fig. 33 of [HPB+93] compares three terms entering into momentum balance: dynamic acceleration (atmospheric motions), sub-grid scale acceleration (Rayleigh friction, convective adjustment, surface drug) and mountain torque acceleration (topography). The mountain torque acceleration makes significant contribution to the momentum balance only near the surface, where it is comparable to the sub-grid scale acceleration and is of the order of 30% of the dynamic

acceleration. Thus, it can be expected that in the absence of topography the increase in the strength of the surface winds will be of the order of 100% and the increase in the strength of the low level mean meridional circulation will be of the order of 30%. The effect of topography on the circulation might be incorporated into the LOM by assuming varying Rayleigh friction coefficient (see Section 2.9.3).

The circulation is derived from the zonal-mean daily averaged diabatic heating rate Q, which is due to net solar radiation. The heating is given by:

$$Q = -\frac{T - T^e}{t_r} \tag{2.6}$$

where T^e is the diurnaly and zonally averaged radiative-convective equilibrium temperature and t_r is a radiative damping time. t_r is assumed to be spatially uniform. Its value is discussed in Section 2.8. Both T^e and t_r depend on the amount of dust present in the atmosphere. In addition, T^e varies with season. The simplified approach by which T^e and t_r depend on dust optical depth is outlined in Section 2.4. Following the conventional definition of the radiative damping time [Hou86], t_r is modeled as

$$t_r = \tilde{t_r} \left(\frac{p_s}{\tilde{p_s}}\right) \left(\frac{\tilde{T}}{T}\right)^3 \tag{2.7}$$

where $\tilde{t_r}$, $\tilde{p_s}$ and $\tilde{T}$ are the values of the radiative damping time, surface pressure and atmospheric temperature at perihelion, respectively. $\tilde{t_r}$ contains most of the dependence on dust optical depth, while scaled pressure and temperature terms contain seasonal variability.

The continuity equation (Eq. 2.5) allows one to introduce a mass stream function ψ in the following way:

$$-v = \frac{g}{2\pi r_m \cos\theta} \frac{\partial \psi}{\partial p} \tag{2.8}$$

$$\omega = \frac{g}{2\pi r_m \cos\theta} \frac{\partial \psi}{\partial y} \tag{2.9}$$

where g is gravity and the units of ψ are kg s^{-1}.

After substituting Eqs. (2.8) and (2.9) into Eqs. (2.1)-(2.3) and making use of Eq. (2.4), the momentum equations and the thermodynamic energy equation can be rewritten in terms of u, ψ, and T only:

$$\left(\frac{\partial}{\partial t}+r\right)u = \lambda\left(\frac{\partial\psi}{\partial p}\frac{\partial u}{\partial y}-\frac{\partial\psi}{\partial y}\frac{\partial u}{\partial p}-\frac{\partial\psi}{\partial p}\left(f+\frac{u\tan\theta}{r_m}\right)\right) \tag{2.10}$$

$$-\lambda\left(\frac{\partial}{\partial t}+r\right)\frac{\partial^2\psi}{\partial p^2} = \frac{\partial}{\partial p}\left(\lambda^2\frac{\partial\psi}{\partial p}\frac{\partial^2\psi}{\partial p\partial y}-\lambda^2\frac{\partial\psi}{\partial y}\frac{\partial^2\psi}{\partial p^2}+u\left(f+\frac{u\tan\theta}{r_m}\right)\right)- -\frac{R}{p}\frac{\partial T}{\partial y} \tag{2.11}$$

$$\left(\frac{\partial}{\partial t}+\frac{1}{t_r}\right)T = -\lambda\left(\frac{\partial\psi}{\partial p}\frac{\partial T}{\partial y}-\frac{\partial\psi}{\partial y}\frac{\partial T}{\partial p}+\frac{\kappa T}{p}\frac{\partial\psi}{\partial y}\right)+\frac{T^e}{t_r} \tag{2.12}$$

where $\lambda \equiv g/(2\pi r_m \cos\theta)$.

2.2.2 Spectral representation

The system of equations (2.10)-(2.12) can be solved by expanding the variables u, ψ and T into a series of weighted basis functions:

$$u(y,p,t) = \sum_i u_i(t)F_i^u(y,p) \tag{2.13}$$

$$\psi(y,p,t) = \sum_i \psi_i(t)F_i^\psi(y,p) \tag{2.14}$$

$$T(y,p,t) = \sum_i T_i(t)F_i^T(y,p) \tag{2.15}$$

where F_i^u, F_i^ψ and F_i^T represent the ith basis function for the fields u, ψ and T respectively and u_i, ψ_i and T_i are the weighting coefficients. Weighting coefficients vary in time, while basis functions vary in space. Boundary conditions for the basis functions assume that $\psi \equiv 0$ on the boundaries of the model domain, which are the southern boundary $\theta = -45°$, the northern boundary $\theta = 45°$, the surface $p = p_s$ and the top of the atmosphere $p = p_t$. The zonal wind $u \equiv 0$ on the lower boundary. With this choice of the boundary conditions there is no mass flow through the boundaries.

With the complete set of basis functions any field can be reproduced. Substitution of the Eqs. (2.13)-(2.15) into the system of partial differential equations (2.10)-(2.12)

converts it into an infinite number of ODEs. Since the goal was to construct a model with the minimum number of ODEs, the basis set was truncated. The truncated basis set was chosen based on the analysis of the u, ψ and T fields generated by the Ames GCM [HPB+93] with the aim of capturing the maximum variance of the system. It will be shown later that the model mimics the GCM to a remarkable extent.

2.2.3 The truncated basis set

The zonal wind u and stream function ψ fields are divided into asymmetric and symmetric parts (relative to the equator), so that $u = \bar{u}_a + \bar{u}_s$ and $\psi = \bar{\psi}_a + \bar{\psi}_s$, and

$$\bar{u}_a = u_a(t) \sin ly(1 + \cos mp')/2 \tag{2.16}$$

$$\bar{u}_s = u_s(t)(A - \cos ly)(1 + \cos mp')/2 \tag{2.17}$$

$$\bar{\psi}_a = \psi_a(t) \sin 2ly \sin mp' \tag{2.18}$$

$$\bar{\psi}_s = \psi_s(t) \cos ly \sin mp' \tag{2.19}$$

$$T = T_{av}(t) + T_{ns}(t) \sin ly + T_v(t) \cos mp' + T_{em}(t) \cos ly \tag{2.20}$$

where

$$\begin{aligned} p' &= p - p_t \\ l &= \pi/2D \\ m &= \pi/(p_s - p_t) \end{aligned}$$

$2D = r_m\pi/2$ is the length of the model domain ($-D \leq y \leq D$) and A is an empirical constant equal to 0.8. The value of A was chosen by comparing the structure of the model's zonal wind field to the one produced by the GCM.

Plots of the basis functions (2.16)-(2.20) are shown on Figs. 2.1, 2.2 and 2.3. Meridional circulation is parallel to the contours of the stream function. The direction of the flow is clockwise around negative values of ψ and counterclockwise around positive values of ψ. ψ_s is positive when air rises in northern hemisphere. ψ_a is

negative when air rises at the equator. Mean zonal winds blowing from west to east (westerlies) are positive and winds blowing from east to west (easterlies) are negative.

The temperature field is made up of the average temperature T_{av}, the horizontal temperature difference $2T_{ns}$ between north and south, the vertical temperature contrast $2T_v$ between lower and upper atmosphere, and the equator-mid latitude temperature difference T_{em}. T_{av} and T_{em} are always positive. T_{ns} is positive when the northern hemisphere is warmer than the southern hemisphere, and T_v is negative when the lower atmosphere is warmer than the upper atmosphere. The atmosphere is convectively stable when the mean atmospheric lapse rate $-dT/dz$ is smaller than the adaibatic lapse rate $\Gamma_a = g/c_p$ [Hou86]. In a stable atmosphere, an air parcel removed from its original position will tend to return to this position, while in an unstable atmosphere it will tend to move away. For Mars, $\Gamma_a = 4.5$ K/km [ZBH+92]. From Fig. 2.3 it appears that the value of T_v^e corresponding to the adiabatic lapse rate in the lower atmosphere is ~ -35 K. However, in the LOM, which deals with variables and parameters that are averaged throughout the atmosphere, the value of T_v^e corresponding to the adiabatic lapse rate corresponds to the value of $-c_4 T_{av} \sim -45$ K. Thus a value of $T_v^e = -35$ K is convectively stable.

The radiative equilibrium temperature T^e (Eq. 2.6) is expanded in the same way as T:

$$T^e = T^e_{av}(t) + T^e_{ns}(t)\sin ly + T^e_v(t)\cos mp + T^e_{em}(t)\cos ly \tag{2.21}$$

2.3 Dust Transport

The transport of dust is governed by the continuity equation:

$$\frac{\partial q}{\partial t} = -v\frac{\partial q}{\partial y} - \omega\frac{\partial q}{\partial p} + S - L \tag{2.22}$$

where q is the dust mixing ratio, and S and L represent sources and sinks of dust, respectively.

For the dust transport equation, the atmosphere is divided into four domains as shown on Fig. 2.4. The average optical depths of the atmospheric domains a, b, c and d are denoted by τ_a, τ_b, τ_c and τ_d, respectively. The average optical depth is

$$\tau_i = \sigma^* \iint_i q \cos\theta dp dy \tag{2.23}$$

where i denotes any of the subscripts a, b, c or d. The proportionality coefficient σ^* is related to the extinction cross section for the dust (assumed constant). The integration extends over the domain i. Optical depths τ_i are used as variables in the model. σ^* and q are only used for consistency in the derivation of the dust transport equation.

There are two reasons for using "boxes" to describe the atmospheric dust distribution, rather than using smooth basis functions as in (2.16)-(2.20). First, it allows one to avoid difficulties in representing surface dust sources with the truncated basis set. When the dust distribution is represented by a truncated set of basis functions, injection of dust into the atmosphere at the lower boundary will have an immediate effect on the dust distribution everywhere in the atmosphere, since the basis functions are continuous throughout the model domain. With the "boxed" representation, the surface dust source affects only the lower atmosphere. Second, the "boxed" representation conserves the amount of dust during advection, while advection of dust in the truncated spectral model may lead to occurrences of negative dust in some parts of the atmosphere.

In the "boxed" representation, the sources of dust exist at the lower boundary of the cells c and d, representing the surface dust source during dust storm activity, and at the upper boundary of the same cells, representing dust gravitationally settling from the cells directly above. Specifics of the surface dust source modeling will be addressed in Section 2.5. The removal of dust from the cells was assumed to be due to gravitational settling only. For simplicity it was modeled as

$$L = -\frac{q}{t_d} \tag{2.24}$$

where t_d is dust fallout time, constant throughout the atmosphere. Numerical values of parameters like t_d are discussed in Section 2.8. Such an approximation of the fallout process assumes strong vertical mixing [Con75].

Rewriting the continuity equation (2.22) in terms of the average optical depths of the corresponding domains, one obtains:

$$\frac{\partial \tau_a}{\partial t} = -\frac{\tau_a}{t_d} + a\bar{\psi}_s(\tau_a - \tau_d)(1-\delta) + a\bar{\psi}_s(\tau_b - \tau_a)\delta \quad (2.25)$$

$$\frac{\partial \tau_b}{\partial t} = -\frac{\tau_b}{t_d} + a\bar{\psi}_s(\tau_b - \tau_a)(1-\delta) + a\bar{\psi}_s(\tau_c - \tau_b)\delta \quad (2.26)$$

$$\frac{\partial \tau_c}{\partial t} = -\frac{\tau_c}{t_d} + \frac{\tau_b}{t_d} + a\bar{\psi}_s(\tau_c - \tau_b)(1-\delta) + a\bar{\psi}_s(\tau_d - \tau_c)\delta + s\delta + s_n \quad (2.27)$$

$$\frac{\partial \tau_d}{\partial t} = -\frac{\tau_d}{t_d} + \frac{\tau_a}{t_d} + a\bar{\psi}_s(\tau_d - \tau_c)(1-\delta) + a\bar{\psi}_s(\tau_a - \tau_d)\delta + s(1-\delta) + s_s \quad (2.28)$$

where

$$\delta = \begin{cases} 0, & \psi_s \geq 0 \\ 1, & \psi_s < 0, \end{cases}$$

$a = g\sqrt{2}/p_s r_m^2 \pi$, s is an interactive dust source at the surface, s_n and s_s are the surface dust sources that are independent of the circulation. The details of the derivation can be found in Appendix A.

In Eqs. (2.25)-(2.28) the terms τ_i/t_d represent dust losses due to gravitational settling (negative terms) or sources of dust from the cell directly above (positive terms). Terms multiplied by $1-\delta$ represent advection of dust by air rising in the SH, while terms multiplied by δ represent advection of dust by air rising in the NH. s_n and s_s represent surface dust sources that are independant of global winds, such as dust devils or local storms. The interactive dust source s is the source for GDSs. It exists only in the hemisphere where air is rising, to account for the observation that during the expansion phase of a GDS dust is entrained into a rising branch of the circuation and carried to high altitudes [LBY+72, AL78].

2.4 Effect of Dust on the Heating Rate

To determine the effects of dust on the heating rate, one can use calculations of the equilibrium temperature fields ([HLP82], Fig. 8–10, 12) which are for the single season $L_s \sim 270°$ (where aerocentric longitude L_s is used as a measure of martian season, $L_s = 270°$ being northern winter solstice) and for uniformly distributed atmospheric dust with total optical depths τ ranging from 0 to 5. These calculations are used to determine the functional dependence of the equilibrium atmospheric temperatures in different regions of the atmosphere (a, b, c and d in Fig. 2.4) on the amount of the atmospheric dust. The seasonal dependence is determined using a simple radiative model. The desired equilibrium temperatures for nonuniform dust distributions and different seasons are then calculated as a product of the function describing the dependence on the atmospheric dust amount and the seasonally varying equilibrium temperatures for clear atmosphere. The dependence of the radiative damping time t_r on dust optical depth is approximated based on the net heating calculations from [PHSL90].

In general, the effect of dust in the atmosphere is to shorten the radiative damping time, to increase T^e_{av}, T^e_{em}, $|T^e_{ns}|$ and to decrease the lapse rate T^e_v. The latter effect levels off for high dust amounts. The seasonal change of T^e_{av}, T^e_{em}, $|T^e_{ns}|$ and T^e_v is about 11% by absolute value between perihelion ($L_s \approx 251°$) and aphelion. In addition, T^e_{ns} term changes sign as the subsolar point switches between the southern and the northern hemispheres.

The details of the heating rate calculation can be found in Appendix B. Comparisons of the LOM's atmospheric fields with the GCM results for different seasons and dust loadings show considerable similarity (see Section 2.9). This lends credence to the method by which the heating was calculated.

2.5 Surface dust source

Once the surface winds exceed a certain threshold speed, sand-size particles become mobilized by winds and are transported by *saltation* [Bag41, GI85]. The surface friction speed U^* is defined as

$$U^* = \sqrt{\tau/\rho} \tag{2.29}$$

where τ is surface shear stress and ρ is fluid density. U^* can be related to the free stream velocity U by the following relationship [Sch55]:

$$U^* = UC_f \tag{2.30}$$

where C_f is a skin-friction coefficient. The saltation threshold speed U_t^* is the "lowest friction speed at which continuous motion of grains is possible" [GI85]. It depends on the particle size, increasing with size for large particles (due to increase in mass), and decreasing with size for smaller particles (due to aerodynamic effects and interparticle forces) [GWP+76]. Thus the minimum threshold velocity is for an intermediate particle size. Figure 2.5 shows the threshold friction velocity dependence on particle size calculated for conditions appropriate for Mars. The curve on Fig. 2.5 was calculated using the formula given in [IW82] with particle density $\rho_p = 2.65 \cdot 10^3\ kg/m^3$, atmospheric density $\rho_a = 2 \cdot 10^{-2}\ kg/m^3$ and viscosity $\nu = 11.19 \cdot 10^4\ m^2/s$. The threshold friction velocity for the most easily moved particles ($\sim 100\ \mu m$) is about 1.5 m/s. The threshold friction velocity needed to raise dust particles (1-20 μm) observed in suspension during a GDS is much greater – $\sim 4\ \mathrm{m}s^{-1}$. Observations by the VLs suggest that surface winds are not strong enough to carry dust particles directly into suspension. Instead, the impact of saltating sand particles on the surface can lead to the raising and suspension of the dust particles [AGM+83, RSL81].

For the dust source s in Eqs. (2.25)-(2.28) the formula for the horizontal particle flux derived in [Whi79] was used:

$$G = s_0 U^{*3}(1 - R)(1 + R^2) \tag{2.31}$$

where G is the horizontal flux of particles of a given size, s_0 is a model parameter, and

$$R = U_t^*/U^*,$$

where U^* is the surface friction speed and U_t^* is the threshold surface friction speed. The flux G is equal to zero when U^* is below the threshold surface friction speed U_t^* ($R \geq 1$) and tends to $s_0 U^{*3}$ as $U^* \to \infty$ ($R \to 0$). Equation (2.31) is used to calculate the vertical dust flux in the LOM since observations suggest that the vertical flux is linearly proportional to the horizontal flux [SRF93]. The value of s_0 is a model parameter and is discussed below.

The total flux s is then a sum over the size distribution of saltating particles weighted by their areal abundance:

$$s = s_0 U^{*3} \int_{D_p} (1 - R)(1 + R^2)\, dS_{rel}\, dD_p \tag{2.32}$$

where s is in units of optical depth per second, S_{rel} is the relative area covered by particles of the diameter D_p,

$$\int dS_{rel}\, dD_p = 1$$

The intensity of the dust source s varies significantly depending on the particle size distribution through the dependence on U_t^*. Figure 2.6 shows the normalized particle flux $s/s_0 U^{*3}$ for two size distributions. The solid line is for the most easily moved particles covering the whole saltating area (Particle Size Distribution 1 or PSD1). At the saltation threshold ($R = 1$) the normalized flux of particles is 0, and at the limit of infinite speed ($R = 0$) the normalized flux is 1. The dashed line corresponds to the case when particles of the sizes from 20 to 2000 μm cover equal surfaces in saltating area (Particle Size Distribution 2 or PSD2). The intensity of the source is much weaker for R close to 1, since only particles with threshold speed close to the minimum threshold speed are going into saltation. As the surface friction speed increases ($R \to 0$) all particles become involved in the saltation process and the normalized flux reaches its maximum (at $R \approx 0.22$). It is thus clear that the particle

size distribution has a profound effect on the intensity of the source, especially for friction velocities just above the threshold value.

Since the surface winds in the LOM are equal to zero, the surface friction speed U^* was assumed to be proportional to the free stream speed, the coefficient of proportionality being absorbed by the parameter s_0. As a proxy for the friction speed the dimensionless quantity

$$U^* = \sqrt{\left(\overline{|u_a| + |u_s|}\right)^2 + \left(\overline{|\psi_a| + |\psi_s|}\right)^2} \tag{2.33}$$

was used. Here the overbar indicates normalization. The zonal winds were normalized to the quantity $(\Omega r_m/2) \approx 120$ m s^{-1} and the stream functions were normalized to 10^{10} kg s^{-1}. These normalization quantities were chosen somewhat arbitrarily so that maximum values at clear conditions of the functions $\overline{|u_a| + |u_s|}$ and $\overline{|\psi_a| + |\psi_s|}$ are of order 1. The zonal and meridional winds thus make approximately equal contributions into U^*, and the value of the dimensionless variable U^* is of order 1. Since I want dust storms to occur only when the wind is close to its maximum value, the threshold friction speed U_t^* is assumed to be a dimensionless parameter of order 1.

The amplitude of the dust source s_0 is assumed to be in units of optical depth per second. For convenience, s and s_0 are scaled by unit optical depth and the characteristic time scale t_d. The dimensionless value of s_0 is used throughout the rest of the thesis as a model parameter.

In this paragraph I show that for s_0 of order 1 the dust flux in the LOM during a GDS is comparable to the constant dust flux used in the GCM to simulate a GDS [MPH+95]. To convert the dimensionless dust flux s in the LOM to units of kg $m^{-2}s^{-1}$, used in the GCM, the flux s is divided by the characteristic time scale t_d and by the extinction cross section for the dust σ:

$$\tilde{s} = \frac{s}{\sigma t_d} \tag{2.34}$$

where $\tilde{s}$ is flux in units of kg $m^{-2}s^{-1}$, σ is in units of $m^2\,kg^{-1}$ and s is given by Eq.

(2.32) with dimensionless parameters s_0, U_t^* and U^*. The flux s during a GDS can be estimated for by assuming $U_t^* \approx 1$ and $U^* \approx 2U_t^*$. From Fig. 2.6 the dimensionless flux is then $s \approx s_0 U^{*3} \approx s_0 8$ for PSD1. The extinction cross section σ can be estimated as the ratio of the geometric cross section of the dust particle to its mass:

$$\sigma = \frac{\pi R_p^2}{4/3\pi R_p^3 \rho_p} \tag{2.35}$$

where R_p is particle radius and ρ_p is particle density. Assuming $R_p \approx 10\mu m$ and $\rho_p \approx 3 \cdot 10^3$ kg m^{-3} for silicate particles, $\sigma \approx 25\ m^2\, kg^{-1}$. Substituting the values for s, σ and $t_d = 25$ sols (see Section 2.8) into Eq. (2.34) yields:

$$\tilde{s} \approx s_0 \frac{8}{25 \cdot 25 \cdot 8.9 \cdot 10^4} \approx s_0 1.4 \cdot 10^{-7} kg\, m^{-2} s^{-1} \tag{2.36}$$

The magnitude of the constant dust source used to simulate GDS in the GCM [MPH+95] was $1.54 \cdot 10^{-7}$ kg $m^{-2}s^{-1}$. Thus, for the chosen scaling $U_t^* \sim 1$ and $t_d = 25$ sols, the dust flux in the LOM is comparable to the dust flux in the GCM if the dimensionless amplitude of the dust source s_0 is of order 1.

The dust source is turned on once the value of U^* exceeds U_t^*. The dust source is then calculated each time step according to Eq. (2.31) and substituted into Eqs. (2.25)-(2.28).

2.6 Projection

The LOM is constructed by Galerkin projection of Eqs. (2.10)-(2.12) and (2.25)-(2.28) onto the truncated basis set (2.16)-(2.20). The resulting system is a set of 12 ODEs for the model variables u_a, u_s, ψ_a, ψ_s, T_{av}, T_{ns}, T_v, T_{em}, τ_a, τ_b, τ_c and τ_d. The equations of the reduced model are given in Appendix C.

As in [Lor63] the truncated basis set is a set of trigonometric functions, chosen for their simplicity. It is not a set of empirical orthogonal functions (EOF), that are often used in construction of LOMs, so there is no guaranty that the resulting LOM is the best approximation of the original model. However, comparison of the

meteorological fields generated by LOM with the GCM simulations (see Section 2.9) shows remarkable similarity, which justifies the choice of the truncated basis set.

2.7 Numerical Method

The model was integrated using a fourth order Runge Kutta scheme. The time step of integration was fixed at 0.4185 of a sol (martian day). Simulations with the time step reduced by a factor of 2 or 4 show no significant difference, except in the initialization phase of the runs and in several special cases, when the model became computationally unstable. The computational method failed when friction in the model (governed by the parameter r in Eqs. (2.10)-(2.12)) was chosen to be too small or too large. The same sensitivity towards parameterized friction was noted in previous models [HLP82].

2.8 Parameter Values

The parameters of the LOM are: r - parameterized friction, t_r – radiative damping time, t_d – dust fallout time, T^e_{av} – spatially averaged equilibrium temperature, T^e_{ns} – half of the hemispheric equilibrium temperature difference, T^e_v – half of the equilibrium temperature contrast between lower and upper atmosphere, T^e_{em} – equator-mid latitude equilibrium temperature difference, s_0 – amplitude of the dust source, U^*_t – threshold surface friction speed.

The value of the friction parameter r (or, conversely, of the frictional decay time $1/r$) was determined empirically by matching the LOM meteorological fields to GCM results for clear conditions. The best results were achieved for $1/r = 5$ sols. This value of r is consistent with the values of parameterized friction used in other models [HLP82]. Radiative damping time for clear conditions was taken to be 2 sols [ZBH+92]. The dust fallout time was estimated by different authors from observations of GDS decay and on theoretical grounds to be of the order of 60 sols [Con75, PCF+79, HLP82]. Since in the model presented here t_d represents the fallout

time through half of the atmosphere, t_d is equal to 30 sols. Note, that t_d is the decay time without circulation, while GDSs observations give the decay time affected by circulation. The estimates of the values of the equilibrium temperature components were obtained from analysis of the 2D GCM calculations of the radiative-convective fields [HLP82]. Due to some ambiguity in determining the parameter values, a range of values is given. The values of model parameters are: $T^e_{av} \sim 180$ to 210 K, $T^e_{ns} \sim 10$ to 20 K, $T^e_v \sim -25$ to -35 K, $T^e_{em} \sim 1$ to 3 K.

The parameters s_0 and U^*_t are dimensionless and of order unity (see Section 2.5). They were varied to achieve the desired result (i.e., GDSs or interannual variability), and will be discussed later.

2.9 Comparison to GCM

The mass stream function, zonal wind and temperature fields produced by the LOM were compared to the Ames GCM results for four seasons and for a range of optical depths ($\tau = 0.3 - 5$). The parameters of the LOM were tuned to fit GCM results. In the simulations with constant dust loading, the interactive dust source s in the LOM was turned off and constant values of τ_a, τ_b, τ_c and τ_d were assumed. After the set of parameters was established, the LOM with interactive dust source was used to simulate a GDS and the results were again compared to the observations [CPH89].

It was possible to reproduce the GCM results reasonably well with one set of parameters for all seasons, except for southern winter solstice (L_s=90°) (see below Section 2.9.3).

Results for southern fall equinox (L_s=0°) and southern spring equinox (L_s=180°) are in general quite similar to each other both in the LOM and the GCM. Thus only results for L_s=0° are shown.

2.9.1 Southern summer solstice, $L_s = 270°$, $\tau = 0.3 - 5$

Figures 2.7-2.12 compare results of the LOM and GCM simulations for this season. The model parameters are: $1/r = 5$ sols, $t_r = 2$ sols, $T^e_{av} = 195$ K, $T^e_{ns} = 15$ K,

$T_v^e = -35$ K, $T_{em}^e = 2$ K. Dust is uniformly distributed throughout the atmosphere. Dust optical depth and distribution are not affected by the circulation. The figures show meridional cross section of the meteorological fields of interest. The negative values are shaded. The structure of the merdional circulation is shown on the upper panel. It consists of one cross-equatorial Hadley cell with its rising branch in the SH and descending branch in NH. The maximum value of the mass stream function is close to $-1.0 \cdot 10^{10}$ kg s^{-1} for $\tau = 0.3$ and close to $-1.5 \cdot 10^{10}$ kg s^{-1} for $\tau = 5$ in the LOM (Figs. 2.7 and 2.11). The zonal winds and temperature fields are shown on the middle and lower panels, respectively. The zonal winds are easterly (from the east) in the SH and westerly (from the west) in the NH. The strength of the winds increases with height in accordance with the thermal wind balance. There is a broad easterly jet with a maximum at about 40°S and a westerly jet with a maximum at the northern border of the model domain (consistent with the polar jet at $\sim 60 - 70$°N in the GCM simulations - see Figs. 2.8, 2.10 and 2.12 reproduced from [HPB+93]). The magnitude of the easterly jet increases in the LOM from ~ 70 m s^{-1} for $\tau = 0.3$ to ~ 100 m s^{-1} for $\tau = 5$. The strongest westerlies in the NH in the LOM increase from ~ 80 ms^{-1} to ~ 120 m s^{-1} for the same values of the optical depth. The highest temperatures at this season occur near surface in SH (230-240 K). The lowest temperatures are in the upper atmosphere above the NH (170-200 K). As the dust loading increases, the temperatures become higher, the atmospheric static stability increases and meridional temperature gradient becomes larger.

Although LOM fields show much less structure than the GCM fields, the overall similarity is quite remarkable. The LOM reproduces reasonably well the location and strength of the zonal jets, the strength, structure and width of the meridional Hadley cell, and the structure of the temperature fields. The differences can be attributed to the lower spatial resolution of the LOM, assumed flat topography and simplified treatment of the effects of dust on atmospheric heating. Qualitatively, the LOM does not reproduce the weak Hadley cell at high southern latitudes and the Ferrel cell at high northern latitudes - because they are outside the model domain. And it does not reproduce the surface westerly jet in the SH - because its scale is smaller than can

be reproduced by the zonal winds basis functions. The sharp temperature gradient near the polar cap is not reproduced by the LOM since the model domain does not extend far enough into the winter hemisphere. Finally, the temperature increase in the upper atmosphere in the NH (due to compressional heating in the descending branch of the Hadley cell) is not seen in LOM simulation. Quantitatively, the LOM matches quite well the strength of the Hadley cell ($\sim -1.0 \cdot 10^{10}$ kg s^{-1} for $\tau = 0.3$ and $\sim -1.5 \cdot 10^{10}$ kg s^{-1} for $\tau = 5$ for the GCM) and zonal jets (the magnitude of the easterly jet in the GCM increases from 60 m s^{-1} to 120 m s^{-1} for $\tau = 0.3$ and $\tau = 5$, respectively, while maximum westerlies at the boundary of the LOM domain increase from $\sim$ 80 m s^{-1} to $\sim$ 100 m s^{-1} for the GCM) (Figs. 2.8 and 2.12). The LOM overestimates the temperatures of the upper atmosphere by about 20 K (lowest temperatures within the LOM domain in the GCM are 170 and 200 K, for $\tau = 0.3$ and $\tau = 5$, respectively).

2.9.2 Southern fall equinox, $L_s = 0°$, $\tau = 0.3$

Zonal winds, temperatures and stream function for southern fall equinox are shown on Fig. 2.13 and Fig. 2.14. The large cross-equatorial Hadley cell of the solsticial circulation is replaced by two weak Hadley cells of comparable strength ($7 \cdot 10^8$ kg s^{-1} in SH and $-5 \cdot 10^8$ kg s^{-1} in NH in the LOM, Fig. 2.13) with a common equatorial rising branch. The pattern of the zonal winds is more symmetrical with a weak ($\sim$5 m s^{-1}) easterly jet above the equator and comparable magnitude westerlies in SH and NH ($\sim$ 30 m s^{-1}) in the LOM. The maxima of the westerly jets are outside the model domain at $\sim$ 60°S and $\sim$ 60°N [HPB+93]. The agreement with the GCM results is again quite remarkable. The LOM reproduces quite well the structure and strength of the westerlies in SH and NH ($\sim$ 60 m s^{-1} and $\sim$ 30 m s^{-1} in the GCM, respectively), and the width and strength of both Hadley cells ($\sim 10 \cdot 10^8$ kg s^{-1} in SH and $\sim -5 \cdot 10^8$ kg s^{-1} in NH for the GCM) (Fig. 2.14). The temperature field captures the overall weaker latitudinal temperature gradient, although the middle atmosphere in the LOM is colder than in the GCM (the 180 K temperature contour

is at $\sim$ 15 km in the LOM and at $\sim$ 25 in the GCM).

2.9.3 Southern winter solstice, $L_s = 90°$, $\tau = 0.3$

The results for the southern winter solstice simulation are shown on Fig. 2.15 and Fig. 2.16. The general structure of the global meteorological fields at southern winter solstice is similar to that at southern summer solstice except for slightly weaker winds and lower temperatures. However, there is a significant discrepancy between the strength of the stream functions in the LOM and GCM simulations. In the GCM simulation the intensity of the Hadley circulation is about a factor of 2 greater during southern summer than during southern winter. In the LOM simulation the difference is smaller - of the order of 30%. The discrepancy is probably due to factors not taken into account by the LOM, such as topography or eddy and wave activity [ZBH$^+$92]. However, the GCM result for southern winter can be reproduced if the friction parameter r is reduced by a factor of 2 (see Fig. 2.17). Thus, it seems reasonable to suggest that the friction parameter is not a constant, but rather a seasonally variable parameter. If this variance is incorporated into the model, every season can be reproduced by LOM with only one set of parameters.

2.9.4 Dust storm

Finally, an experiment with an interactive dust source was performed, and the dust optical depth variation was compared to the VLs observations of the GDS in 1977 [CPH89]. A GDS develops spontaneously in the model for sufficiently small U_t^* and sufficiently large s_0. The amplitude of the dust source and threshold friction speed were varied to achieve the best fit to the observations. Accordingly, the threshold friction speed and amplitude of the dust source were $U_t^* = 1$ and $s_0 = 4.5$ in this experiment. The amplitude of the dust source was chosen so that the maximum optical depth of the storm is above the lower limit on optical depth measured at the VL1 site. The maximum optical depth reached during a GDS scales approximately linearly with the magnitude of the dust source s_0 for this parameter range. At the

same time, the magnitude of the source in the LOM is comparable to the magnitude of the source in the GCM [MPH+95] (see Section 2.5). For this particular choice of U_t^* and s_0, GDSs only occur in the SH near perihelion. Two different particle size distributions, described in Section 2.5, were used. The results are similar, thus only results for the PSD2 are shown. Figure 2.18 compares optical depth changes in the NH simulated by the LOM with measurements at the VL1 and VL2 sites (Clb89). The horizontal axis represents time measured in sols from perihelion ($L_s \approx 250°$). Observations are indicated by $\times$'s, while the LOM simulation is depicted by a solid line. Note that the measurements during the maxima of the dust storms ($t \approx -100$ to 0 sols and $t \approx 25$ to 150 sols) are lower limits. The VL1 and VL2 measurements are at $\theta \approx 23°$N and $\theta \approx 48°$N respectively, while the LOM gives optical depth averaged over the NH. Thus, given the progression of the storm from the south to the north, and the position of the VL1 in the middle of the LOM NH domain, the data for VL1 might be more suitable for comparison with the LOM.

The storm starts near perihelion, which corresponds to the time of maximum insolation. At the beginning of the storm, the optical depth in the NH increases sharply as dust is transported from the SH into the NH. At this initial stage, increased heating due to atmospheric dust in the SH creates a large meridional temperature gradient. The peak value of the stream function increases by a factor of ~ 3 relative to its value at the same season in clear conditions, and reaches $-2.4 \cdot 10^{10}$ kg s^{-1}. The circulation time, calculated as the atmospheric mass divided by the average mass flux, is of the order of 6 sols, which compares very well with the timescale of the dust storm spreading $\sim$10 sols [Mar74, Tho79].

As the storms progresses, dust optical depth reaches its maximum of $\sim$4 in the NH (for comparison, the maximum τ in SH is $\sim$10; this two to one ratio of the maximum optical depth reached in SH and NH compares very well with the 3D GCM simulations of the GDS [MHTP93]). The meridional temperature gradient and the meridional and zonal winds all decrease, because both hemispheres are now equally dusty. The decrease of the winds is also due to a change in planetary orbital position and the corresponding decrease in solar insolation. The dust input diminishes and

GDS enters into the decay phase. The observed dust storm decay continued until the dust optical depth reached value of $\sim$1, at which point the decay slowed down [PCF$^+$79]. It is suggested that this change in the rate of decay is due to the triggering of the local dust raising activity, which maintains the global dust haze at the level of $\tau = 0.3 - 0.7$. Since no such process was included in the LOM, the decay of the simulated storm continued until $\tau = 0$. Nevertheless, the duration of the simulated and observed storms compares very well.

It is evident from the Fig. 2.18 that LOM simulates very well the second GDS. It does not do as well simulating the first GDS. If the value of the threshold friction speed is lowered from $U_t^* = 1.0$ to $U_t^* = 0.5$ in an effort to shift the timing of the storm, GDSs start to occur in the NH during northern summer. The atmosphere becomes permanently dusty and the dust source remains active for the better part of the year. Two dust storms occur every year, one in the SH and one in the NH, and their durations lengthen with decreasing U_t^*. Even if the interactive dust source is turned off in the NH, only one long storm occurs in the SH. It can be made to start at the time of the first storm of 1977, but it develops slower than the observed storm, picks up around perihelion and then slowly decays with the decay time that is much larger then the observed one. Apparently, some kind of a negative feedback between dust source and circulation is needed to shut down the dust source shortly after the start of the first storm, so that two dust storms are possible during southern summer. Some of the mechanisms that were proposed for dust storm decay include: redistribution of dust or saltating particles on the surface [ZBH$^+$92], increased static stability that suppresses surface winds [PCF$^+$79], scavenging of dust by condensing water or CO_2 [PCF$^+$79] and passage through a resonant state of the atmosphere [Til88]. No such mechanisms are present in the LOM. The GDS simulated by the LOM does not need a special mechanism for the dust source to shut down since the intensity of the source decreases as the circulation weakens with the advent of autumn in the SH.

Table 2.1: Coefficients of the functions $f_i(\tau_i)$.

i	q_i	s_i
a	0.23	2.8
b	0.23	2.8
c	0.08	2.6
d	0.08	2.6
r	0.6	1.0

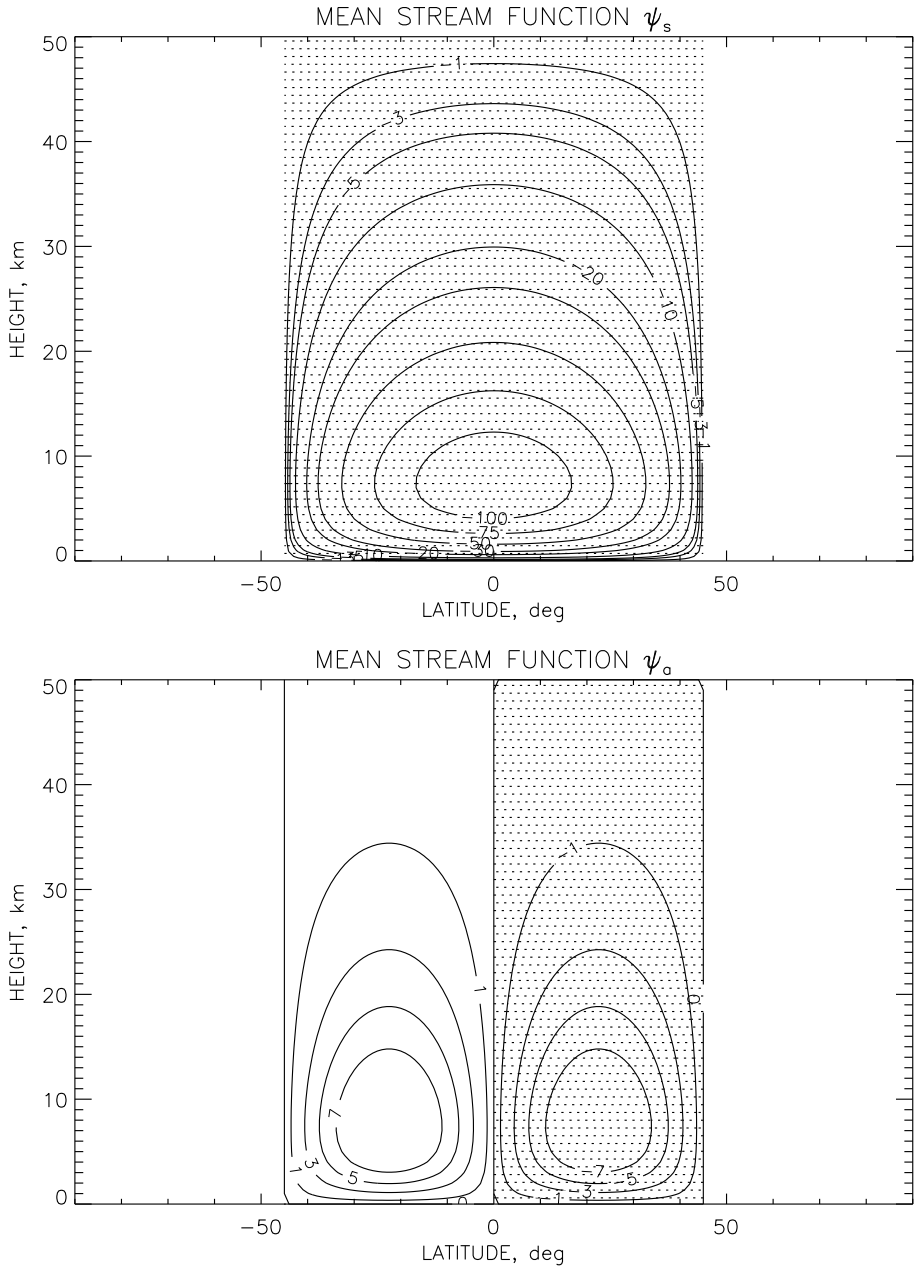

Figure 2.1: Contour plots of the basis functions $\bar{\psi}_s$ and $\bar{\psi}_a$ corresponding to hypothetical values of $\psi_s = -120$ and of $\psi_a = -10$. Negative values are shaded. Flow in the meridional plane is parallel to stream function contours. The direction of the flow is clockwise around negative values and counterclockwise around positive values.

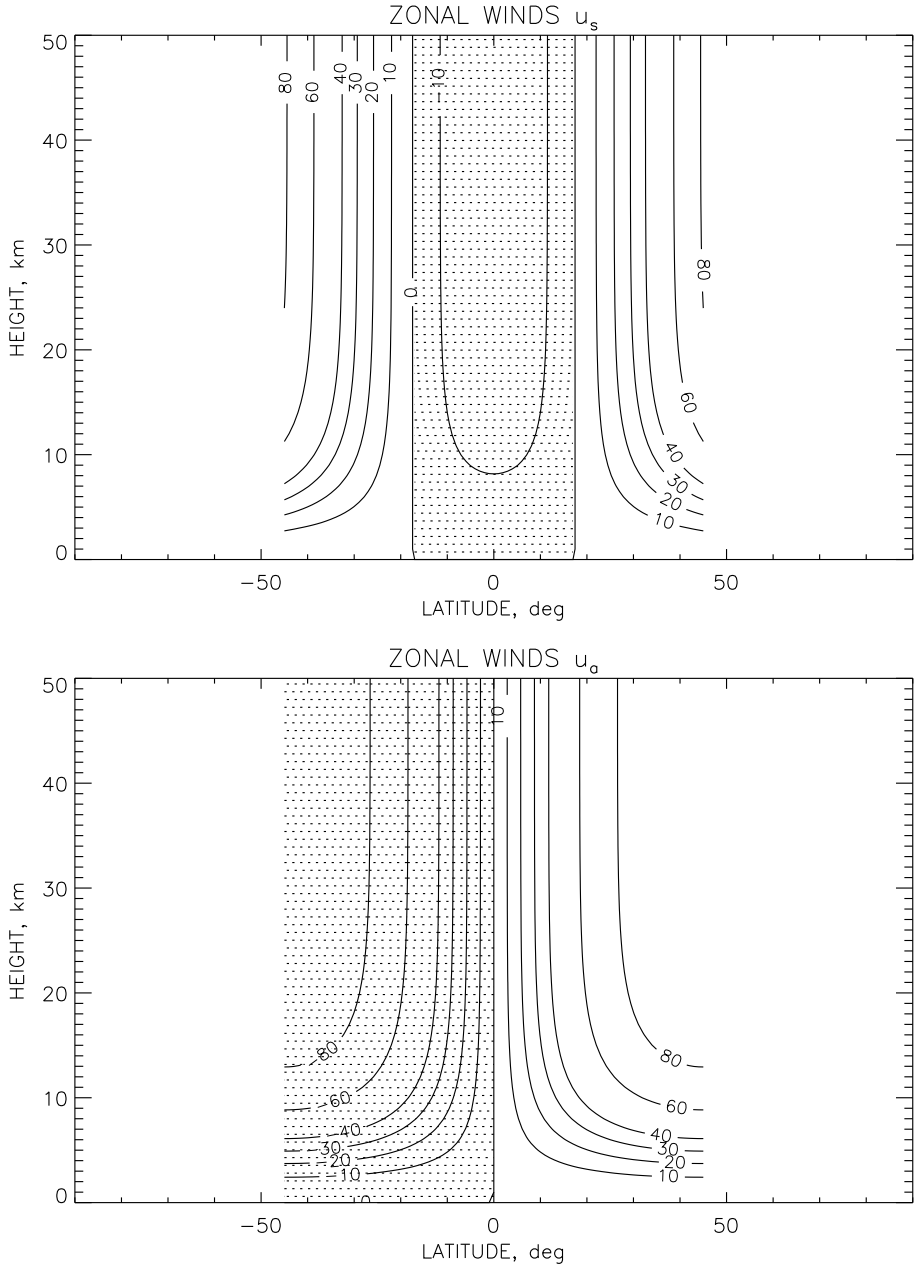

Figure 2.2: Contour plots of the zonal winds basis functions $\bar{u}_s$ and $\bar{u}_a$ corresponding to hypothetical values of $u_s = 100$ m s^{-1} and of $u_a = 100$ m s^{-1}. Negative values are shaded. Negative values correspond to easterly (from the east) winds.

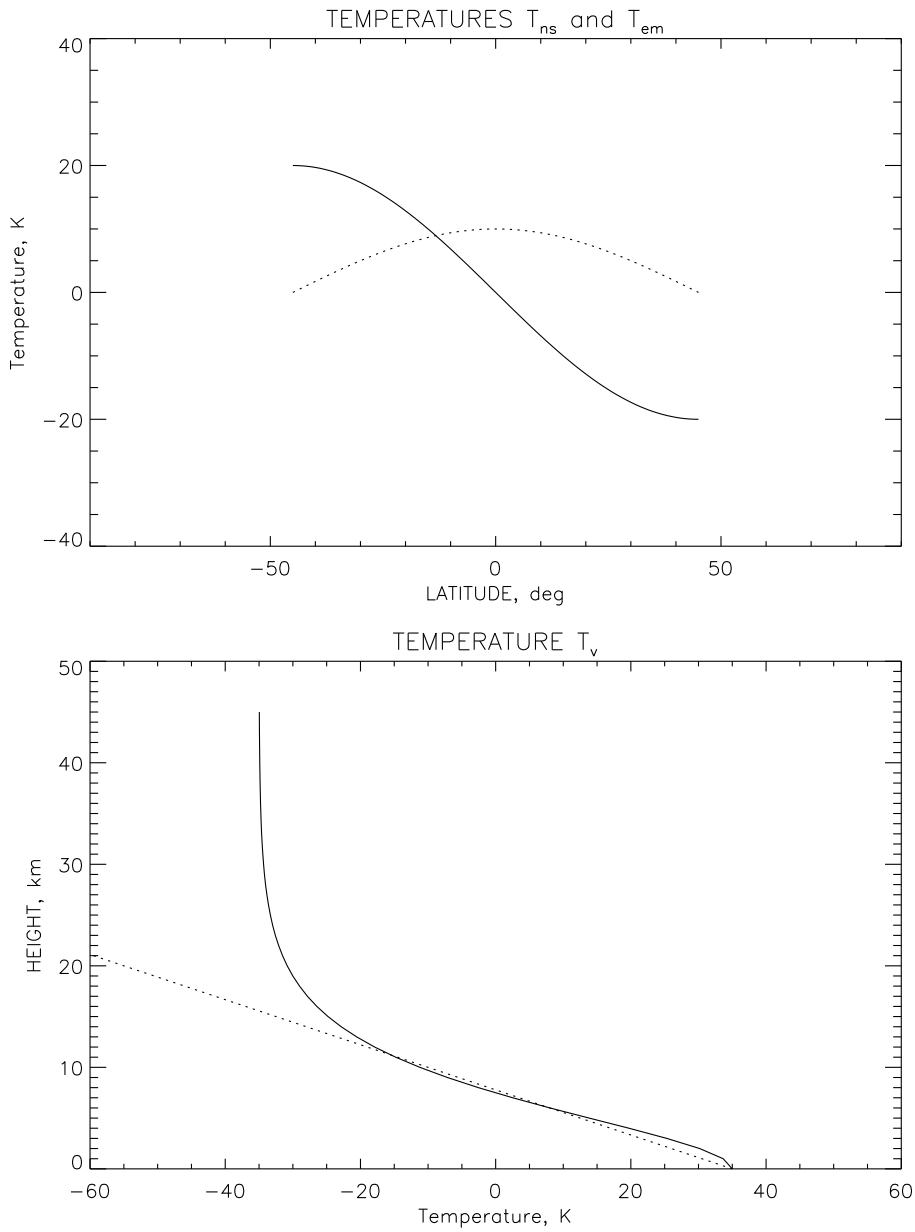

Figure 2.3: Plots of the basis functions T_{ns}, T_v and T_{em} corresponding to hypothetical values of $T_{ns} = -20$ K, of $T_v = -35$ K and of $T_{em} = 10$ K. On the upper panel T_{ns} is shown by solid line and T_{em} is shown by dashed line. On the lower panel T_v is shown by solid line and adiabatic temperature profile ($\Gamma_a = 4.5$ K km^{-1}) is shown by dashed line.

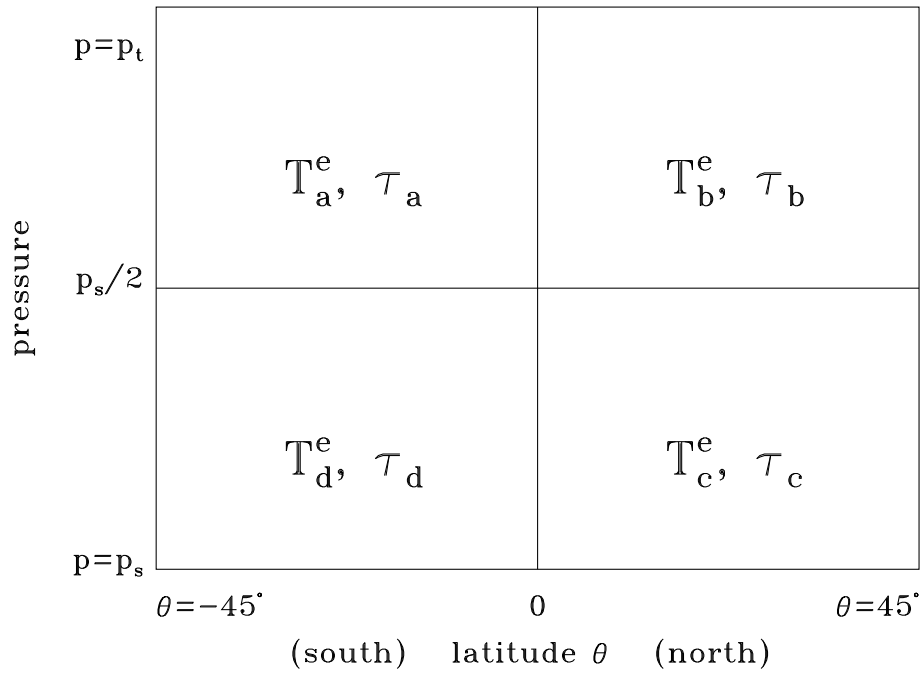

Figure 2.4: Schematic illustration of the subdivision of the atmosphere into four domains used in derivation of dust transport equations and determination of heating rate.

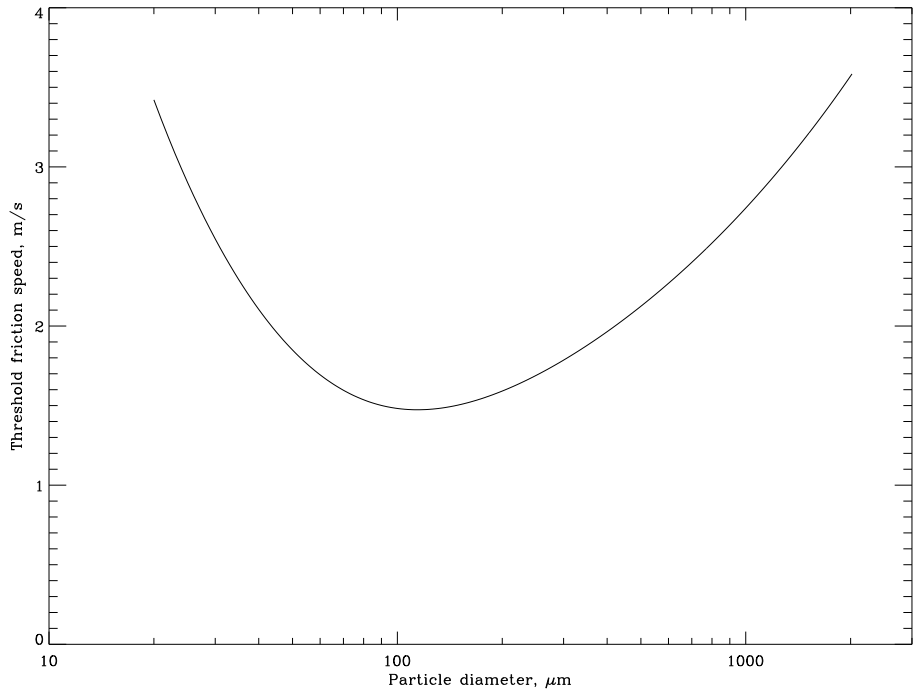

Figure 2.5: Threshold friction speed prediction for Mars according to [IW82].

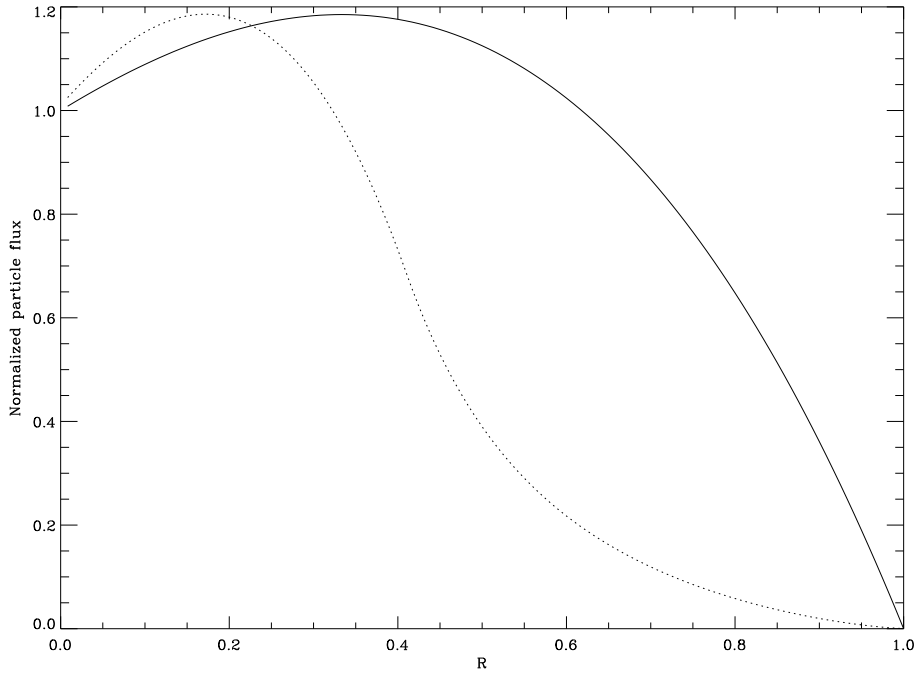

Figure 2.6: Normalized integrated particle flux for two particle size distributions PSD1 and PSD2. The solid line is for the case of the most easily moved particles covering the whole saltating area (PSD1). The dashed line is for the case of particles from 20 to 2000 μm covering equal areas (PSD2). $R = U_t^*/U^*$.

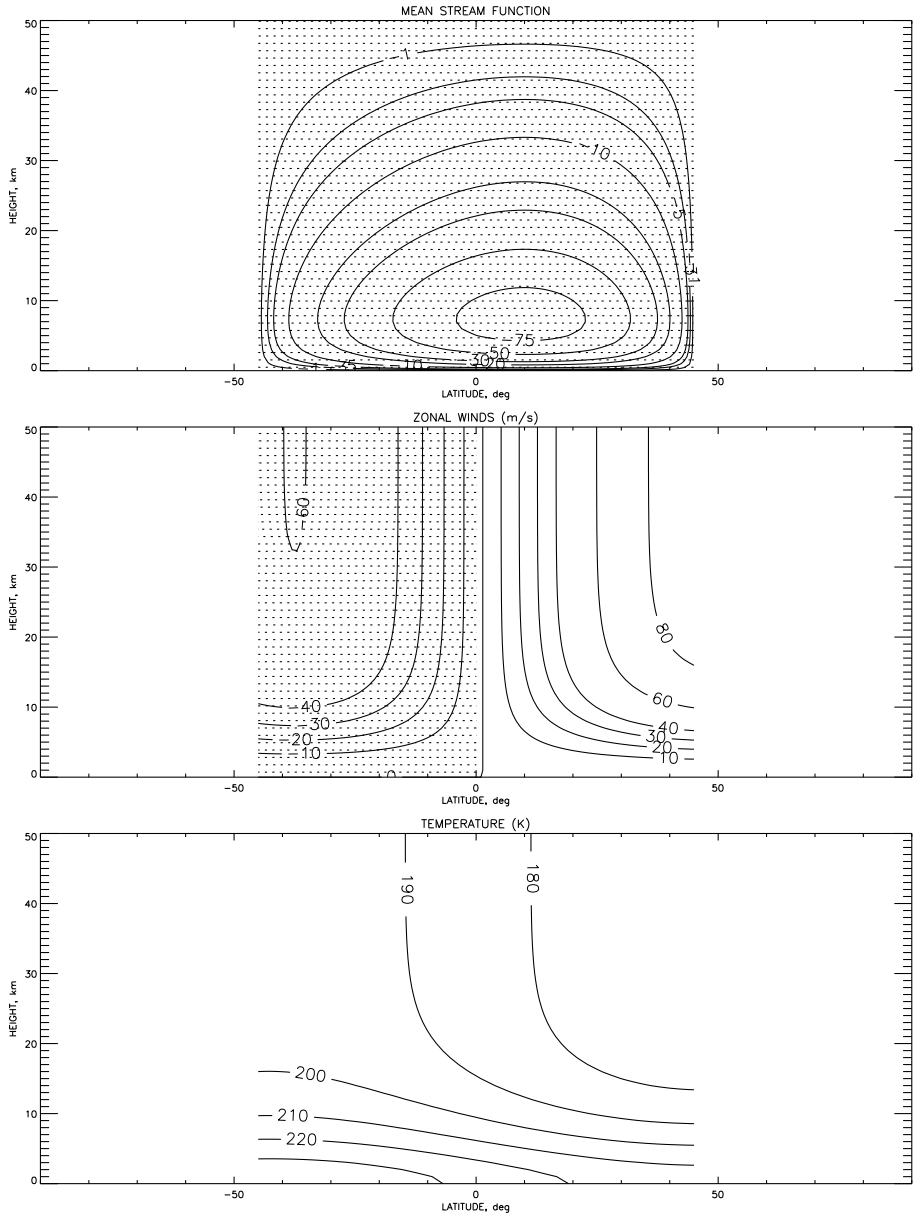

Figure 2.7: LOM simulation of the southern summer solstice. (a) Mass stream function in units of 10^8 kg s^{-1}, (b) zonal winds ($m\,s^{-1}$) and (c) temperatures (K) for southern summer solstice, $L_s = 270°$, $\tau = 0.3$.

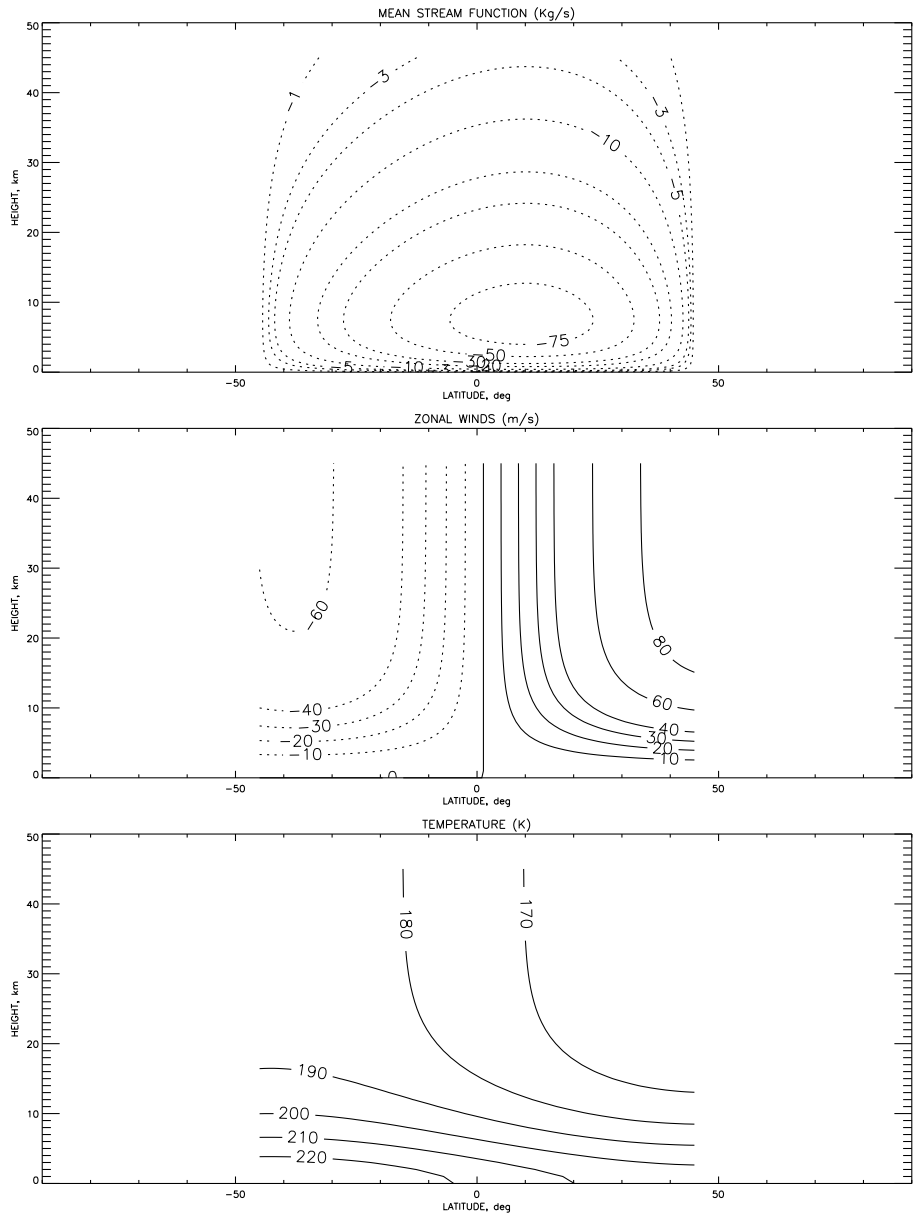

Figure 2.8: GCM simulation of the southern summer solstice. (a) Mass stream function in units of 10^8 kg s^{-1}, (b) zonal winds ($m\,s^{-1}$) and (c) temperatures (K) for southern summer solstice, $L_s = 255° - 286°$, $\tau = 0.3$ ([HPB+93], Figs. 2, 3).

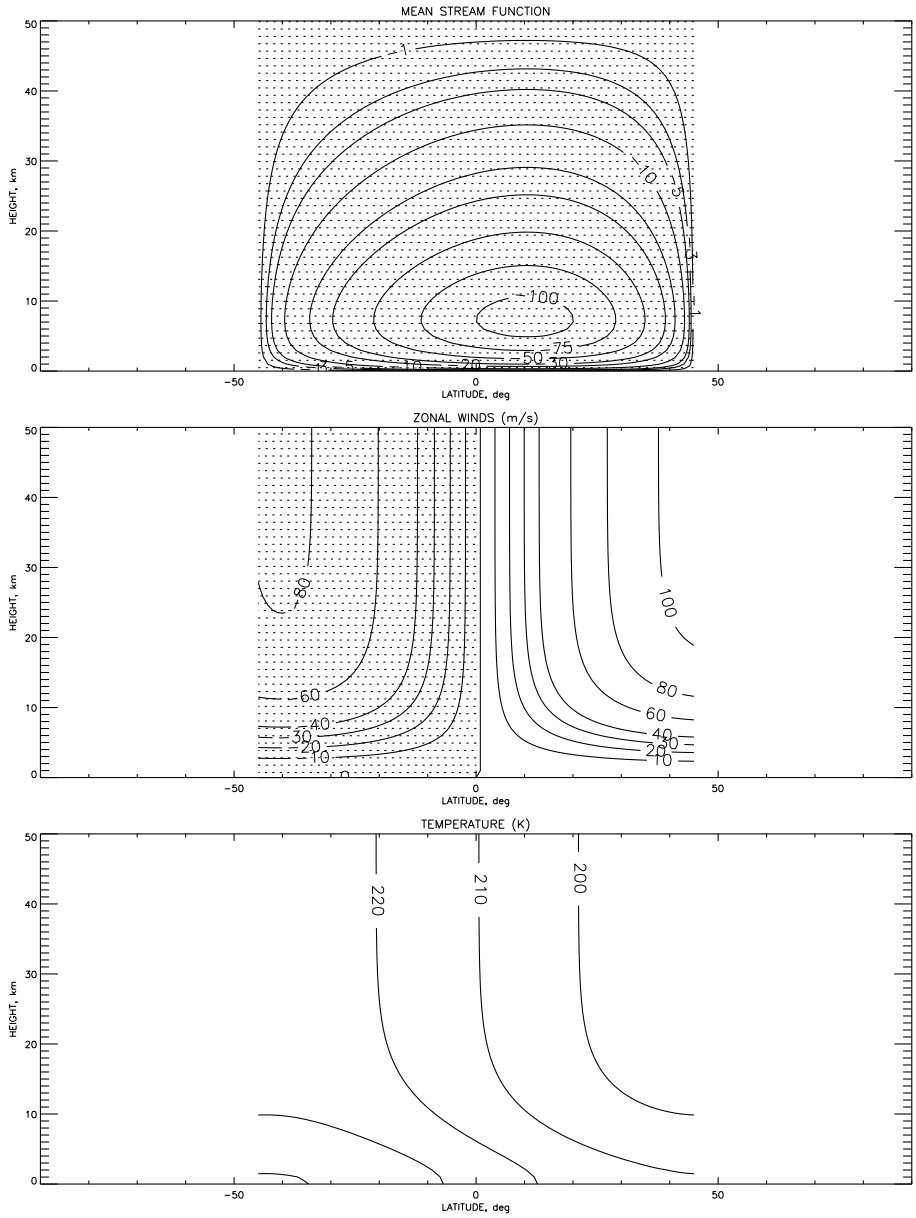

Figure 2.9: Same as Fig. 2.7 but for $\tau = 1$.

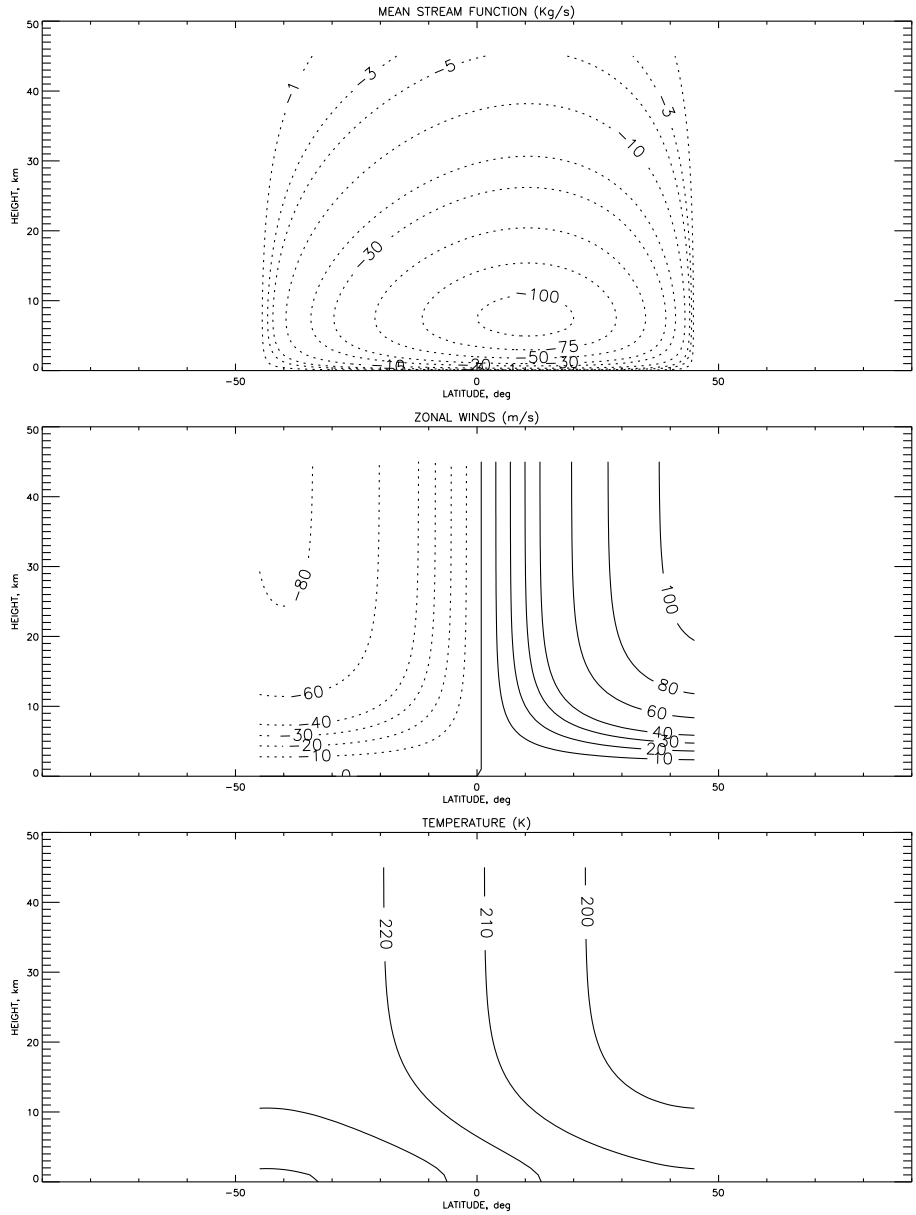

Figure 2.10: Same as Fig. 2.8 but for $\tau = 1$ ([HPB+93], Figs. 5, 7).

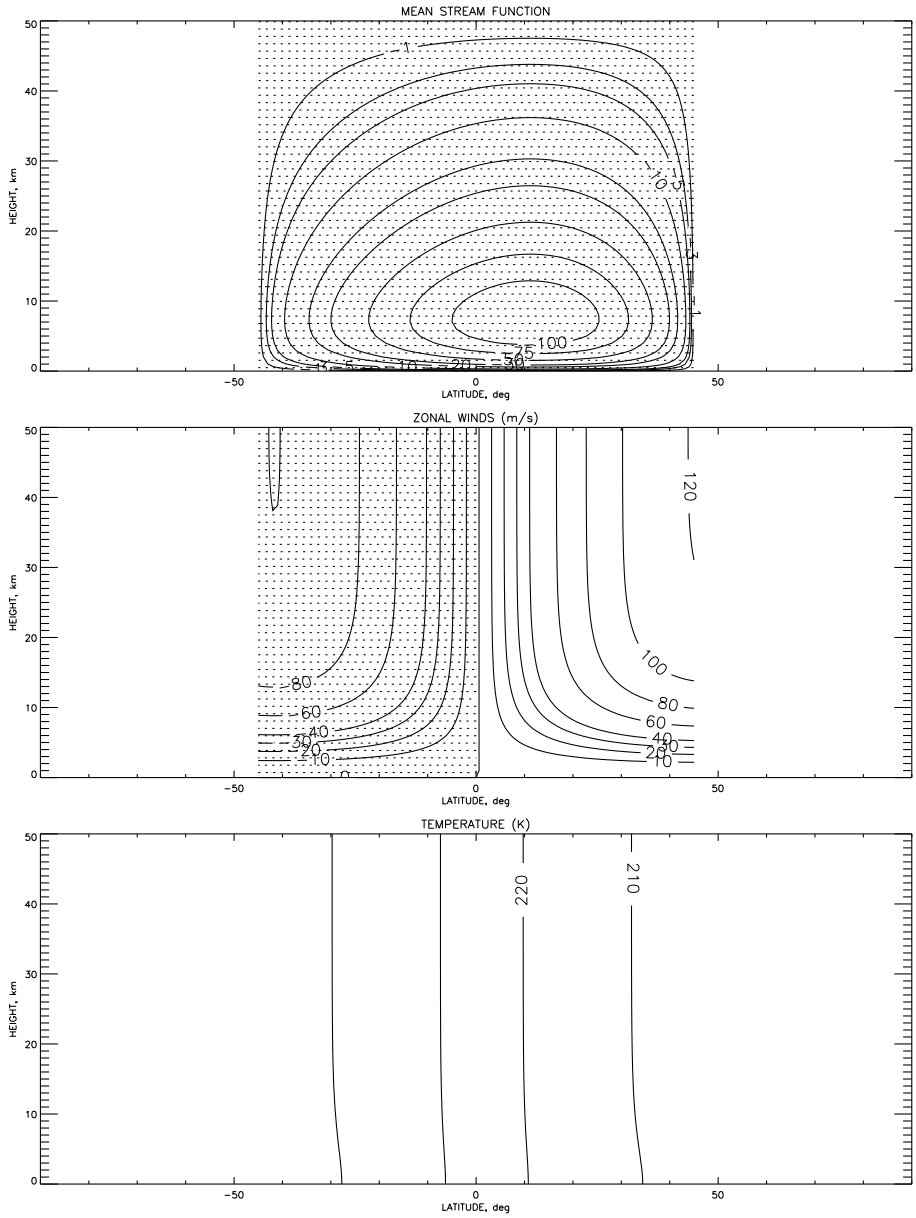

Figure 2.11: Same as Fig. 2.7 but for $\tau = 5$.

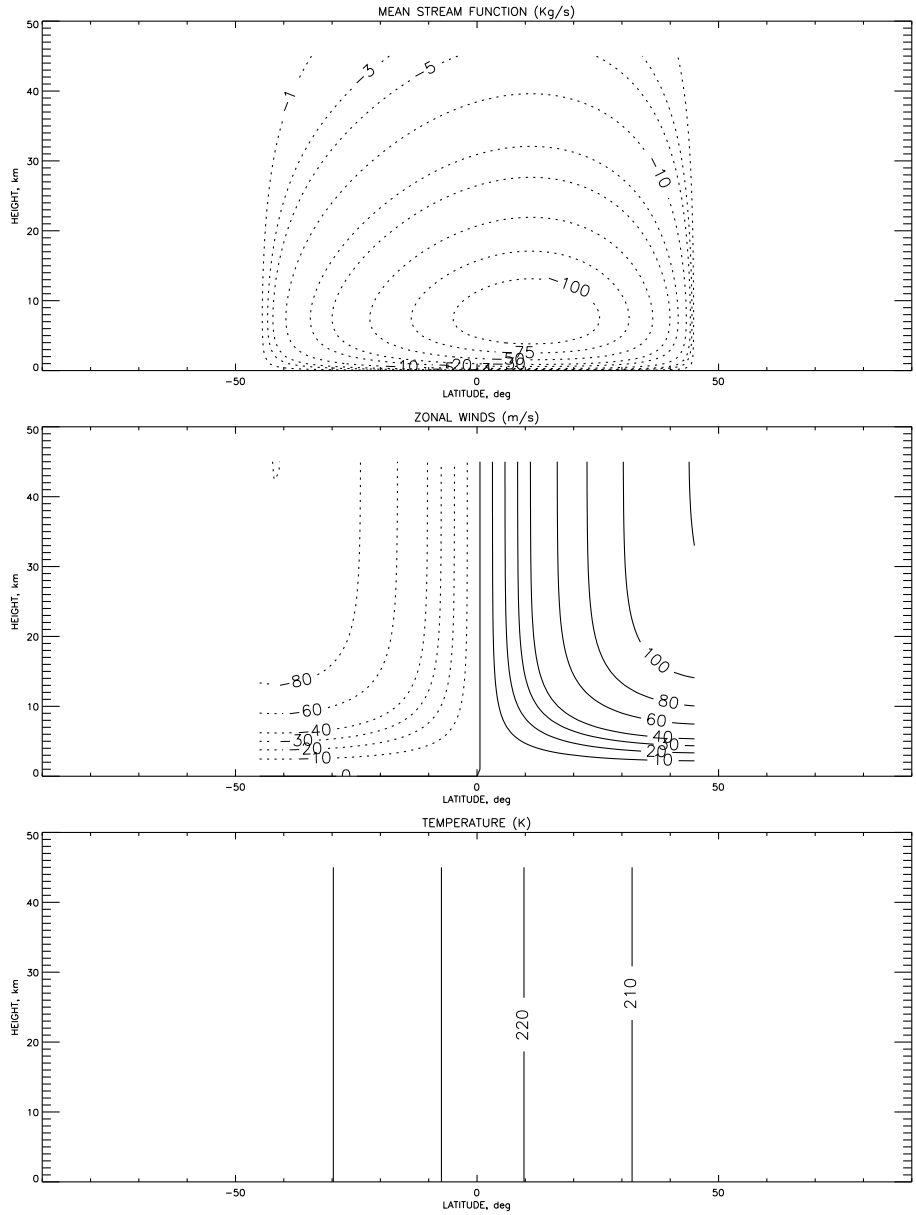

Figure 2.12: Same as Fig. 2.8 but for $\tau = 5$ ([HPB+93], Figs. 6, 8).

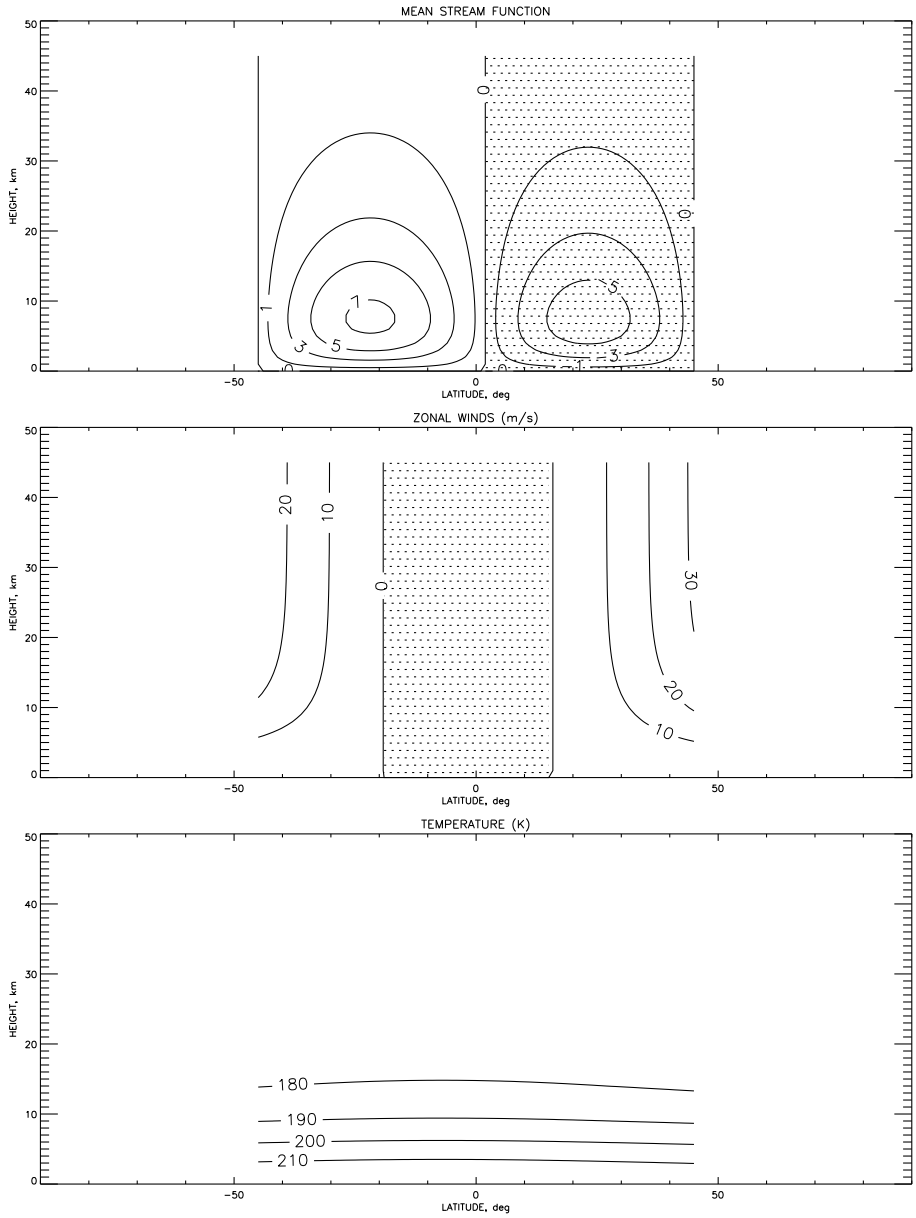

Figure 2.13: Same as Fig. 2.7 but for southern fall equinox, $L_s = 0°$, $\tau = 0.3$.

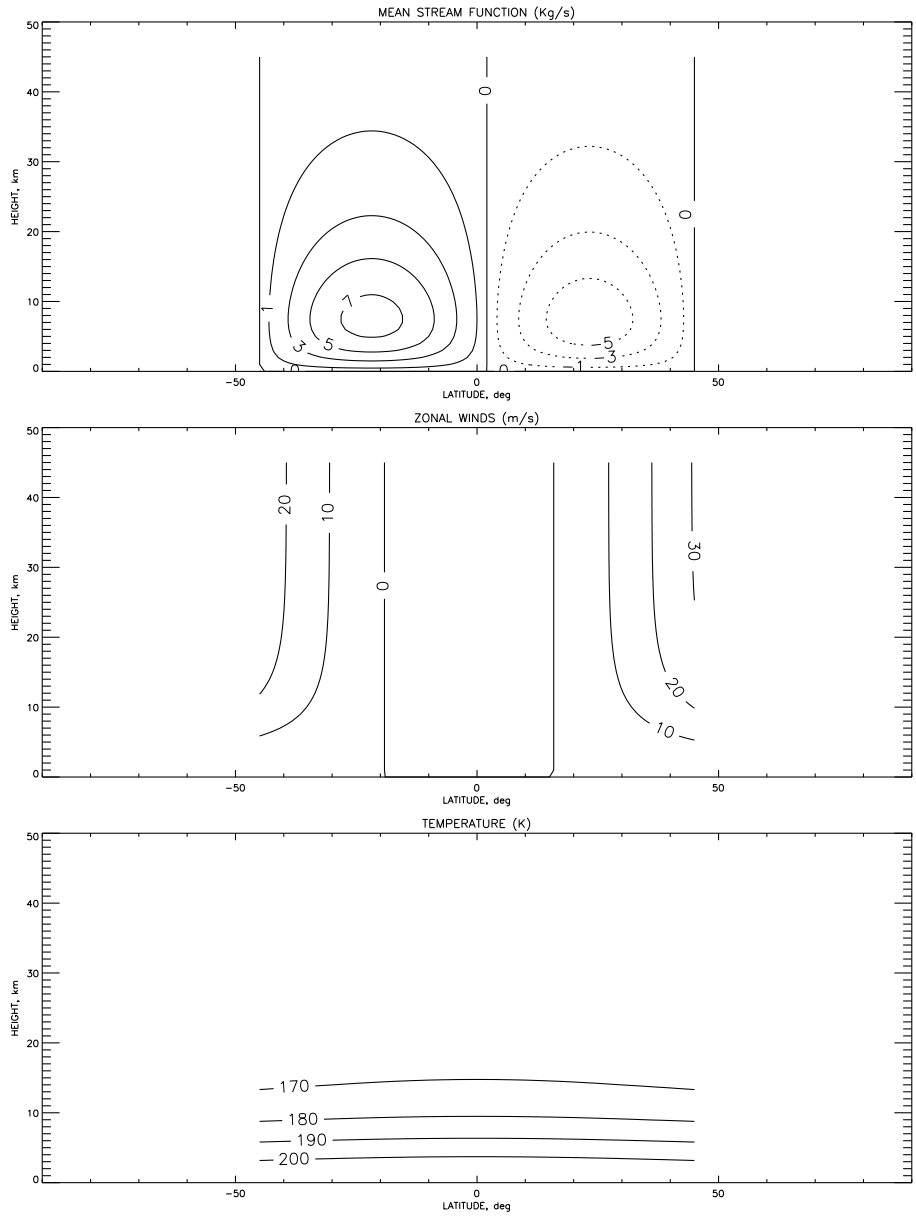

Figure 2.14: Same as Fig. 2.8 but for southern fall equinox, $L_s = 0° - 23°$, $\tau = 0.3$ ([HPB+93], Figs. 11, 13).

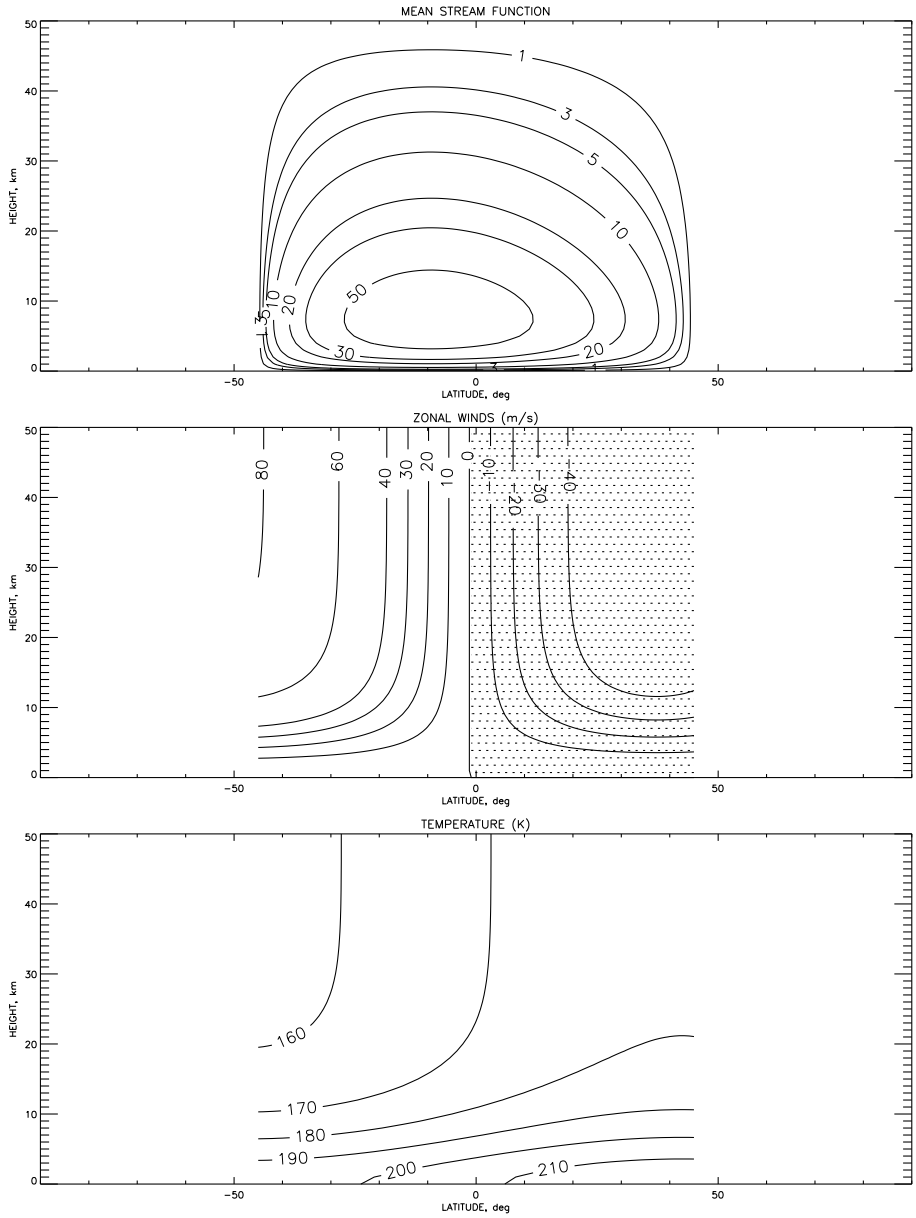

Figure 2.15: Same as Fig. 2.7 but for southern winter solstice, $L_s = 90°$, $\tau = 0.3$.

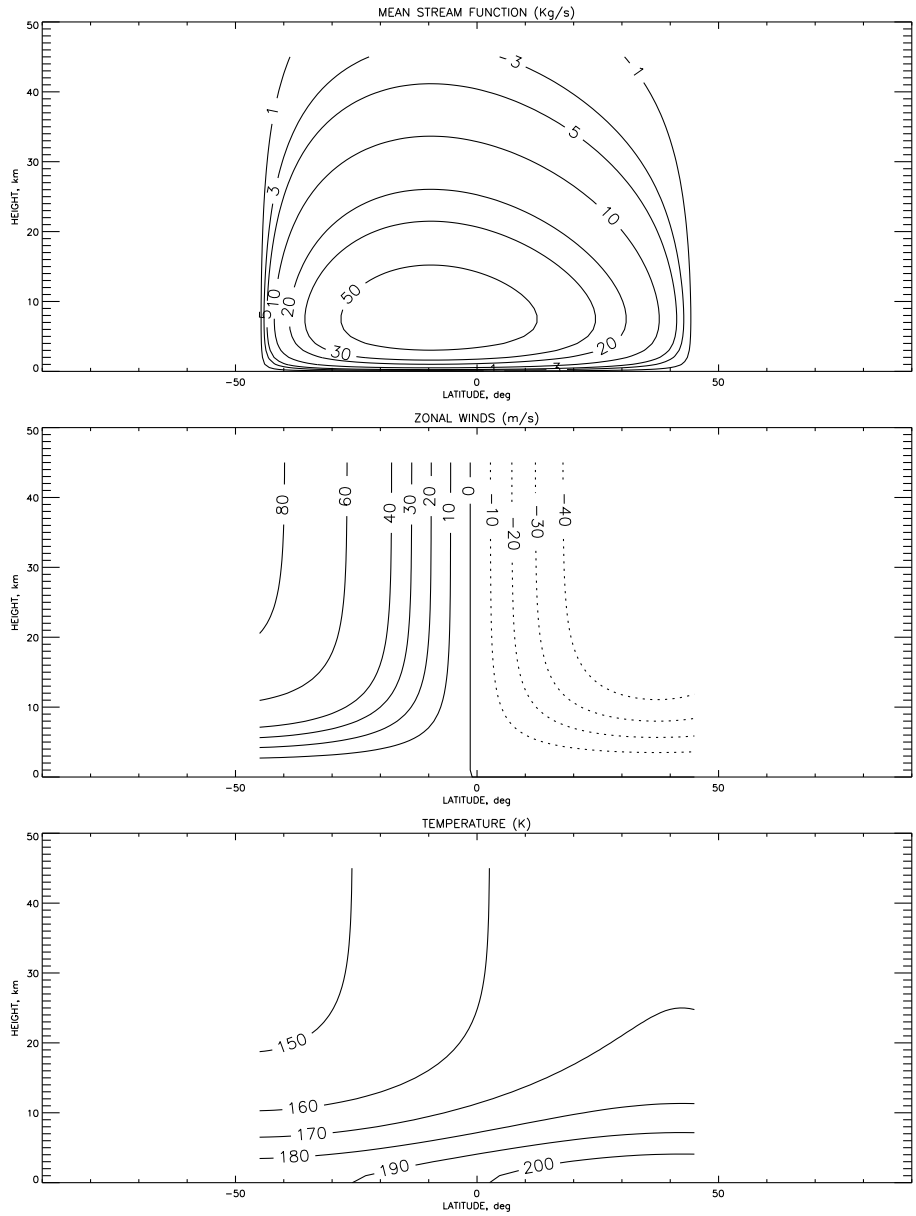

Figure 2.16: Same as Fig. 2.8 but for southern winter solstice, $L_s = 85° - 107°$, $\tau = 0.3$ ([HPB+93], Figs. 9, 10).

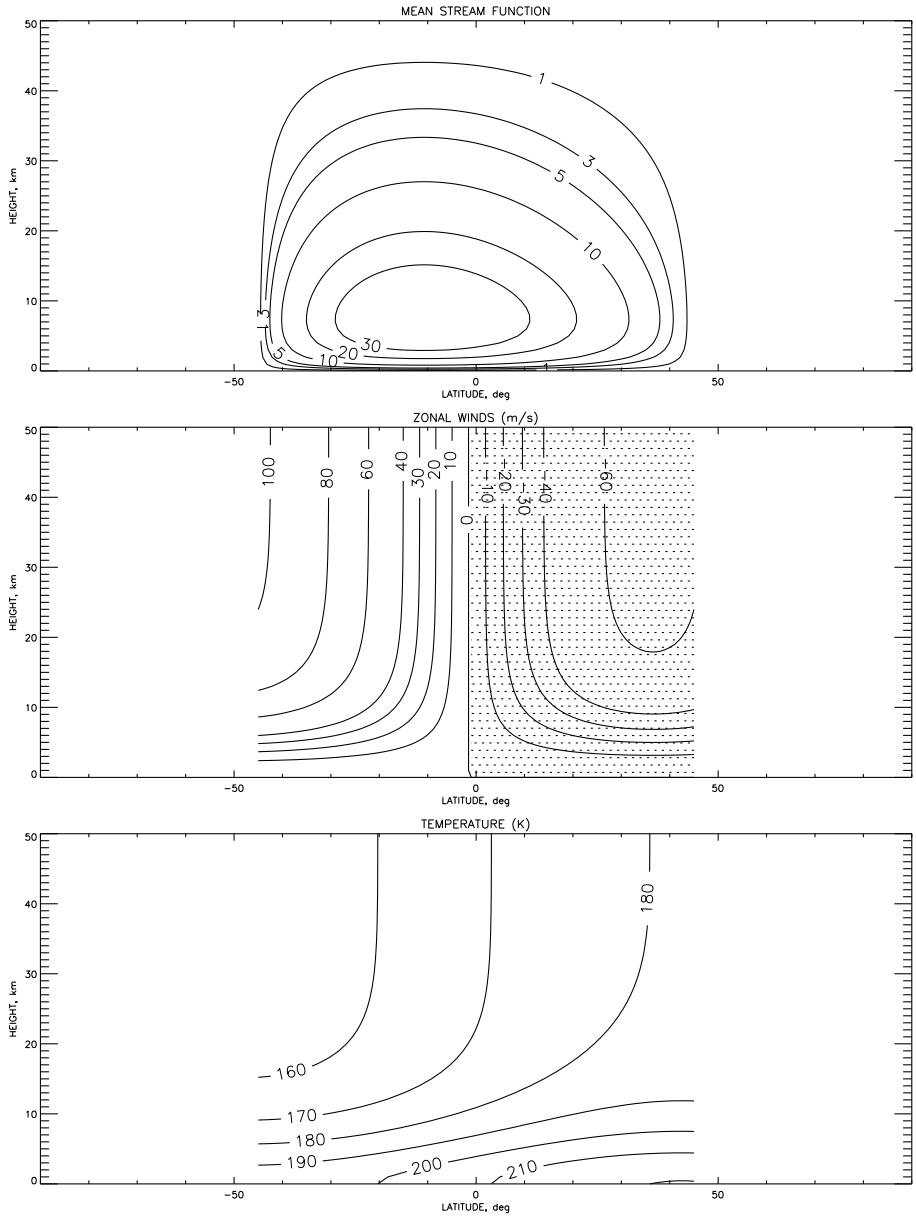

Figure 2.17: Same as Fig. 2.15 but with the friction parameter r reduced by a factor of 2 ($r = 1/10\ sols^{-1}$).

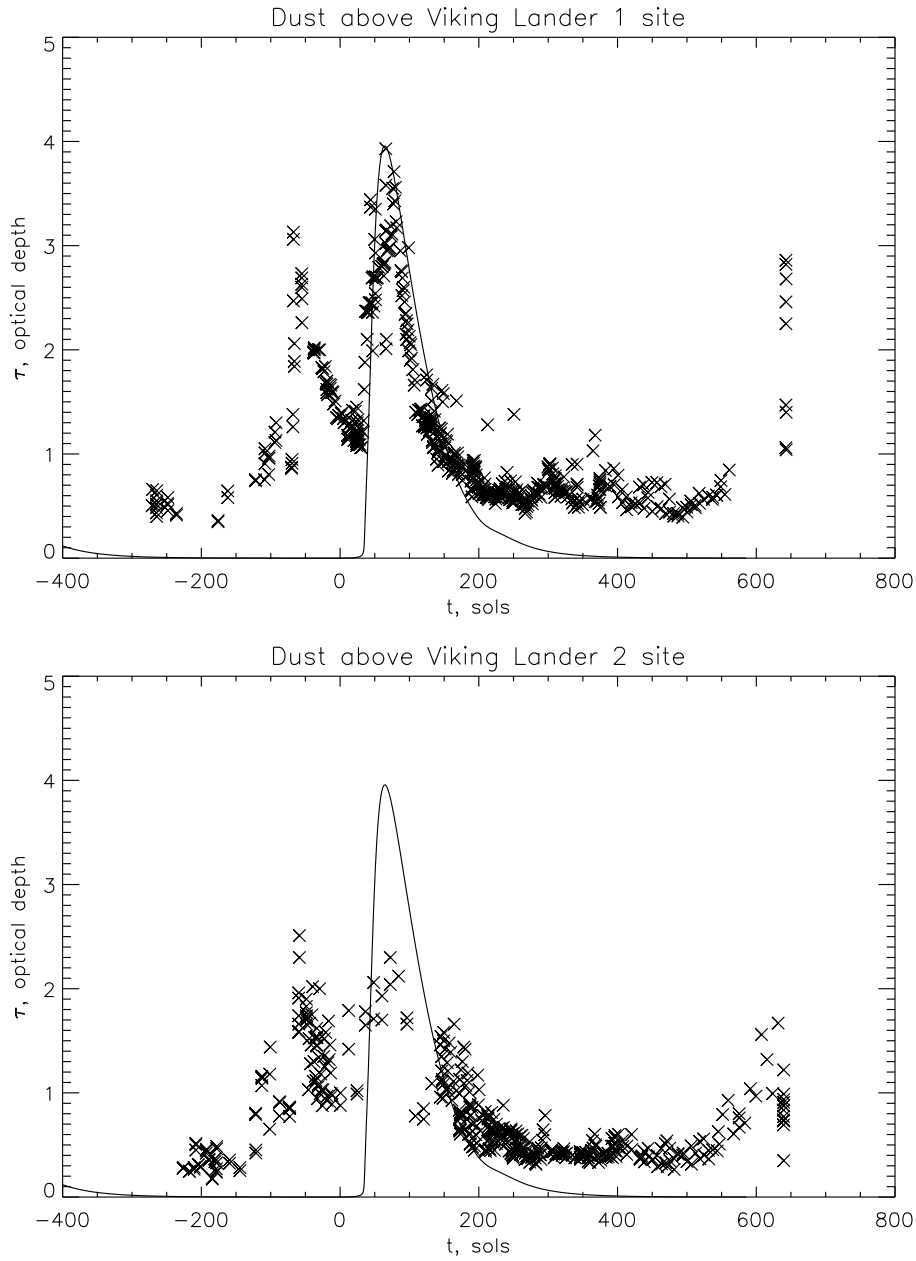

Figure 2.18: Comparison of the LOM GDS simulations and measurements by VL1 and VL2 (from [CPH89]).

Chapter 3 Analogy with the Lorenz System

3.1 Introduction

The LOM described in Chapter 2 has 12 variables and 9 parameters. The model is too complex to be analyzed by any means other than numerical. However, the part of the model describing atmospheric dynamics (i.e., the LOM uncoupled from the dust) can be further simplified and analyzed analytically. The resulting model is a system of three ODEs that links model variables ψ_s, T_{ns} and T_v. This system is the famous Lorenz system [Lor63] with an additional seasonal forcing term.

This result is not very surprising since the original Lorenz system described Rayleigh-Bénard convection, and the Hadley cell is just a huge convection cell (in the first approximation). The very eminence of the Lorenz system is based on its applicability towards climate research [Lor63]. The solutions of the system are known to exhibit chaotic behavior. In the context of the evolution of the climate system this means that small variations in initial conditions can over time lead to significant differences in final states of the system. For Mars, this may mean a difference between years with and without a GDS.

The Lorenz system has been extensively studied [Spa82] and modified to include noise [Fow89], time varying parameters [AHL85, SWB91] and external forcing [FZ95] to better approximate real climate systems. External forcing, for example, may represent the annual or daily cycle in the thermal forcing of the atmosphere. Addition of the external forcing can lead to suppression and creation of chaos [FZ95], depending on model parameters and the amplitude and period of the forcing. However, the modification of the Lorenz system derived in the next Section has not been previously described in the literature. The forcing term is added to a different equation, which

changes the symmetry of the system. Qualitative analysis of the parameter space and numerical results will be presented. This analysis can be used as a rough guide to the properties of the full LOM.

3.2 Reduction of the Model

The following derivation should not be viewed as a rigorous one, but rather as an easy way to simplify the model, which will be later validated numerically.

With certain assumptions, the LOM reduces to a set of 3 equations in the 3 variables ψ_s, T_{ns} and T_v. Equation C.1 becomes a balance between two quantities (1) the sum of the zonal Coriolis and centrifugal forces on the meridional wind $(a_{11}X_2X_4 - a_{12}X_4)$ and (2) frictional drug on the zonal wind u_a $(-c_1X_1)$. Equation C.4 becomes an equation for the rate of increase of the meridional circulation ψ_s, where the forcing is proportional to the interhemispheric temperature difference T_{ns} $(a_{43}X_6)$. Equations C.6 and C.7 become equations for the rate of change of the interhemispheric temperature difference T_{ns} and vertical temperature difference T_v, respectively, due to advection of heat by the meridional circulation $[-a_{61}X_4(X_7 + c_4X_5)$ and $a_{71}X_4X_6]$ and forcing by diabatic heating $[-c_2(X_6 - F_2)$ and $-c_2(X_7 - F_3)]$.

The assumptions made in the derivation are: the circulation timescale associated with ψ_a is much longer than the timescale of the frictional process $1/r$ and of the radiative cooling t_r; the zonal Coriolis force is much larger than the centrifugal force; T_{em} is much smaller than T_{av}; $\partial u_a/\partial t \approx 0$; and $\partial T_v^e/\partial t \approx 0$. Since the radiative damping time is short, T_{av}^e was used as a proxy for T_{av}. Numerical simulations show that these approximations are valid if $2 < 1/r < 50$ sols and $t_r < 50$ sols.

The resulting system can be written as

$$\dot{X} = -\hat{\sigma}X + \hat{\sigma}Y \tag{3.1}$$

$$\dot{Y} = -Y - XZ + X\hat{r} + F \tag{3.2}$$

$$\dot{Z} = -Z + XY \tag{3.3}$$

where a dot denotes a derivative with respect to the dimensionless time $t' = t/t_r$, and X, Y and Z are dimensionless model variables:

$$X = \psi_s/\bar{\Psi}, \qquad Y = T_{ns}/\bar{T}, \qquad Z = (T_v - T_v^e)/\bar{T}.$$

The scaling coefficients are:

$$\begin{aligned} \bar{\Psi} &= c_2\Psi/a = 1.7\ p_s r_m^2/gt_r \\ \bar{T} &= \left(c_1^2 + a_{12}a_{41}\right) Tc_2/aa_{43}c_1 = 0.9(r^2 + 0.16\ \Omega^2)r_m^2 H/rt_r Rh \end{aligned}$$

where $a = (a_{61} + a_{71})/2$, Ψ and T are the normalization coefficients of the LOM, and indexed coefficients are the coefficients of the LOM (see Appendix C). For typical martian conditions and r not too small ($1/r$ of the order of several sols), $\bar{\Psi} \approx 2.2 \cdot 10^{10}/t_r$ kg s^{-1}, where t_r is in sols, and $\bar{T} \approx 11/t_r r$ K, where t_r is in sols and $1/r$ is in sols.

Parameters of the model are the seasonal forcing F, $\hat{\sigma}$ and $\hat{r}$:

$$\begin{aligned} F &= T_{ns}^e/\bar{T} \\ \hat{\sigma} &= \left(c_1^2 + a_{12}a_{41}\right)/c_1c_2 = (r^2 + 0.16\ \Omega^2)t_r/r \\ \hat{r} &= -\left(T_v^e + c_4 T_{av}^e\right)/\bar{T} = -\left(T_v^e + 0.24T_{av}^e\right)/\bar{T} \end{aligned}$$

For parameter values used in Chapter 2, $\hat{\sigma} \approx 65$, $\hat{r} \approx -0.5$, $F \approx 0.55$. Since T_{av}^e and T_v^e are seasonally dependent, the parameter $\hat{r}$ changes slowly with time. However, since T_{av}^e and T_v^e change "in phase," the time dependence of the parameter $\hat{r}$ is very weak and for practical reasons it can be assumed constant.

Except for the additional term F in the $\dot{Y}$ equation, the system of equations (3.1)-(3.3) is the Lorenz system [Lor63] with his parameter $b = 1$. The $\dot{X}$ equation states that the intensity of the Hadley circulation is governed by dissipation ($-\hat{\sigma}X$) and forcing by the horizontal temperature gradient ($\hat{\sigma}Y$). The parameter $\hat{\sigma}$ defines the dynamical response rate of the system. For $\hat{\sigma}$ large the system responds to

changes almost immidiately compared to the timescale of radiative damping and the forcing F. Evolution of the horizontal temperature gradient Y is described by the $\dot{Y}$ equation. Changes in Y are due to radiative damping $(-Y)$, advection $(-XZ + X\hat{r})$ and seasonal forcing F. The advection term represents advection of the quantity $Z - \hat{r} \sim T_v + c_4\ T_{av}$ by the scaled circulation X. The quantity $Z - \hat{r}$ can be viewed as the scaled atmospheric stability with T_v $(T_v < 0)$ representing the temperature change associated with the mean lapse rate and the quantity $c_4\ T_{av}$ representing the temperature change associated with the adiabatic lapse rate ($c_4\ T_{av} \sim \Gamma_a H \approx 50$ K, where Γ is adiabatic lapse rate and H is scale height). The $\dot{Y}$ equation thus represents a scaled version of the energy balance equation of the nearly inviscid Hadley circulation theory [HH80]. Finally, the $\dot{Z}$ equation states that changes in the scaled vertical temperature gradient Z are due to radiative damping $(-Z)$ and advection of the horizontal temperature gradient (XY).

3.3 Parameter Space Analysis

Because the system of equations (3.1)-(3.3) depends on time explicitly – via the seasonal forcing term $F(t)$, – it belongs to a different class from the original Lorenz system – the nonautonomous systems. The boundedness of the trajectories can be proven in much the same way as in [FZ95]. Furthermore, it is obvious that dissipation and periodic forcing prevent the existence of stationary points or completely unstable periodic orbits. Again, in much the same way as in [FZ95], it can be proven that the only attracting sets that can be found for Eqs. (3.1)-(3.3) are periodic orbits and strange attractors.

3.3.1 Constant forcing

The stability of the solution X, Y, Z of the system (3.1)-(3.3) can be formally analyzed by assuming constant F and considering the behavior of small perturbations of the steady state solution. Experience shows that conclusions made about parameter domains found in this way are applicable to an extent to periodically forced systems,

because the system's behavior differs in each domain [FZ95]. In addition, for the parameter values appropriate for Mars the response time of the system is much shorter than the year, so F is quasi-steady.

The characteristic equation of the constant F system (3.1)-(3.3) is

$$\lambda^3 + [\hat{\sigma} + 2]\lambda^2 + [1 + \hat{\sigma}(2 - \hat{r}) + X^2(1 + \hat{\sigma})]\lambda + \hat{\sigma}[1 + 3X^2 - \hat{r}] = 0 \qquad (3.4)$$

where λ is the Lyapunov exponent. The Lyapunov exponent describes the rate of growth (decay) of small disturbance of the initial condition. X in Eq. (3.4) is the steady state solution of the Eqs. (3.1)-(3.3):

$$F = X\left(X^2 + 1 - \hat{r}\right) \qquad (3.5)$$

$$Y = X \qquad (3.6)$$

$$Z = X^2 \qquad (3.7)$$

The solution is given in term of X, rather than in terms of F for the sake of simplicity. Equation 3.5 can be solved analytically to give $X(F)$, but the result will be described by a complex formula.

Solutions of Eq. (3.4) depend on the parameters $\hat{\sigma}$, $\hat{r}$ and on the forcing F. Depending on the values of these parameters, the solutions of the Eqs. (3.1)-(3.3) can be stable or unstable. The following qualitative analysis of the parameter space is for $\hat{\sigma} \gg 1$, for the sake of comparison with the LOM described in the previous Chapter.

Graphic representation of the Eq. (3.5) is given on Fig. 3.1. Steady state solutions are given by intersection of the line $F = const$ and the curve $F(X)$. The solid curve is for $\hat{r} = -0.5$ (corresponding to parameter values used in Chapter 2 and also representative of the solutions with $\hat{r} < 1$) and the dashed curve is for $\hat{r} = 3$ (representative of the solutions with $\hat{r} > 1$). It is clear from Fig. 3.1 that the system (3.1)-(3.3) has only one steady state solution for $\hat{r} < 1$ (solid curve) for any given F,

and three solutions for $\hat{r} > 1$ (dashed curve) and $F_- \leq F \leq F_+$, where

$$F_+ = -F_- = \frac{2}{3}\left(\frac{\hat{r}-1}{3}\right)^{3/2} \tag{3.8}$$

are the local extrema of the dashed curve. Letters A, D mark regions of stability and B, C mark boundaries of the region of instability on the dashed curve.

Analysis of the solutions of Eq. (3.4) shows that for $\hat{r} \leq 1$ it has three roots with negative real parts, and the solution given by Eqs. (3.5)-(3.7) is always stable.

If $\hat{r}$ is increased above 1, one of the roots has positive real part for $B \leq X \leq C$. For $\hat{r}$ slightly above 1, B and C correspond to the local extrema of the dashed curve on Fig. 3.1. For larger $\hat{r}$, B moves along the curve towards more negative X's and C moves towards more positive X's. Numerical integration of the system (3.1)-(3.3) with constant forcing shows that solutions within this region are unstable and the system quickly switches to the stable branch of the curve (to branch A for $B \leq X \leq C$ and $F \leq 0$ and to branch D for $F \geq 0$).

For $\hat{r} \geq \hat{r}_{crit}$, where $\hat{r}_{crit}$ is the original Lorenz critical value of $\hat{r}$ for the onset of unsteady convection (with $b = 1$):

$$\hat{r}_{crit} = \sigma(\sigma + 4)(\sigma - 2)^{-1}$$

Eq. (3.4) possesses complex roots in the vicinity of points B and C. For $B \leq X \leq C$ the real parts of those roots are positive and solutions oscillate and grow with time. Numerical experiments show that the system (3.1)-(3.3) with constant forcing exhibits aperiodic behavior for sufficiently small F and $\hat{r} \geq \hat{r}_{crit}$. Figure 3.2 illustrates the behavior of the system in this regime. The figure shows a time series of the model variable X for the first 80 sols of simulation, corresponding to 2,000 iterations. The model parameters are: $\hat{\sigma} = 10$, $\hat{r} = 25$ and $F = 0.9$. The critical value of $\hat{r}$ in this case is $\hat{r}_{crit} = 17.5$, hence $\hat{r} > \hat{r}_{crit}$. The variable X, as well as the model variables Y and Z (not shown), undergo seemingly chaotic oscillations. Recall, however, that the parameter values used in Chapter 2 give $\hat{r} \approx -0.5$.

3.3.2 Periodic forcing

When the external forcing F is periodic, the behavior of the system (3.1)-(3.3) depends on the frequency of the forcing. The response of the system can be changed significantly (compared to the case of constant F) if the forcing frequency is near the system's eigenfrequency or its multiples [FZ95]. Here analysis is restricted to the forcing with the annual frequency. It can be expected that the frequency of the forcing will not have a noticable effect on the behavior of the model, since it is much lower than the frequency of the model's free oscillations (see Fig. 3.2).

For $\hat{r} \leq 1$ the system remains stable under the periodic forcing. The state of the system, which can be represented by a point on (F, X) plane, follows the forcing F along the curve $F(X)$ (solid curve on Fig. 3.1). The solid curve thus represents the trajectory of the state of system on the (F, X) plane.

For $1 \leq \hat{r} \leq \hat{r}_{crit}$ an interesting phenomenon is observed in the behavior of the system. The state of the system again can be found on or near the curve $F(X)$ for $X < B$ and $X > C$. However, as the system approaches the point B from the left or point C from the right, it switches to the stable branch – to D from the vicinity of B and to A from the vicinity of C. This kind of behavior of the system is illustrated on Fig. 3.3 (compare to Fig. 3.1). The dotted curve represents the steady state solutions of Eqs. (3.1)-(3.3) for $\hat{\sigma} = 65$, $\hat{r} = 3$. The solid curve represents the trajectory of the state of the system in the (F, X) plane calculated for $F = 1.6$ and annual frequency. The time progression is clockwise along the solid curve. As the system switches between branches, it exhibits damped oscillations with frequency higher than the annual frequency. The behavior of the system, however, is periodic.

Another interesting phenomenon, characteristic of the parameter regime $\hat{r} \geq 1$, occurs when the amplitude of the forcing F is smaller than $F_+ = -F_-$ (Eq. (3.8)). In this case, depending on the initial state of the system, it will remain on either branch A or D, without switching to the other branch every season. Physically, this would mean that the same hemisphere is always warmer than the other, and air continues to rise in the same hemisphere, despite the normal progression of the seasons.

For $\hat{r} \geq \hat{r}_{crit}$ and for small F, chaos persists in the system. For larger F, mixed behavior is observed – periodic oscillations near the extrema of $F(t)$ and chaos near $F(t) \approx 0$. An example of such mixed behavior is shown on Fig. 3.4. The figure shows time series of the model variable X (rapidly oscillationg curve) overlaped on the $F(t)$ (smooth curve) for $\hat{\sigma} = 10$, $\hat{r} = 25$ and $F = 5$. The same simulation with constant forcing produces a stable solution.

The above analysis of the parameter space is by no means complete. However, the results agree well with similar studies [FZ95] and allow one to make a number of conclusions regarding the behavior of the LOM.

3.4 Behavior of the Uncoupled LOM

To validate the derivation of the simplified model (3.1)-(3.3), its results were compared to results of the full LOM without dust (uncoupled LOM). Figure 3.5 shows plots of time series of the stream function ψ_s and of the temperatures T_{ns} and $-T_v$ calculated with two models with parameter values used in Chapter 2. Solid lines indicate calculations with Eqs. (3.1)-(3.3) and dashed lines indicate calculations with the uncoupled LOM. The time series start at $t = 0.75$ martian year to exclude the spin-up oscillations at the start of the run. A year starts at perihelion ($L_s \approx 251°$). Negative values of ψ_s correspond to air rising in the SH and positive values correspond to air rising in the NH. Negative values of T_{ns} correspond to warmer SH and positive values correspond to warmer NH.

As can be seen from the figure, the Lorenz system approximates the LOM quite well. The biggest discrepancy is during the peak of southern summer and the peak of northern summer. The simplified model tends to overestimate the intensity of the circulation compared to the LOM during this period by $\sim$ 10%. The discrepancy between temperatures is much smaller – of the order of a percent. Thus, the results of the analysis of Section 3.3 can be extended to the uncoupled LOM. The behavior of the coupled LOM will be addressed in Part II of the thesis.

The system of Eqs. (3.1)-(3.3) allows one to analyze the subspace of solutions of

the LOM pertaining to the variables ψ_s, T_{ns} and T_v. It is, however, possible that the rest of the model variables comprise a separate system that might possess chaotic solutions in the relevant parameter range. The analysis of Section 3.3 thus must be viewed as a rough guide to the properties of the uncoupled LOM. Theoretical conclusions have to be validated by numerical calculations. If these conclusions are valid for a number of parameters, they are probably valid everywhere in the parameter space.

For the set of parameters appropriate for Mars, $\hat{\sigma} \approx 65$, $\hat{r} \approx -0.5$, $F \approx 0.55$. From the above analysis it follows that the system is stable, since the control parameter $\hat{r}$ is much smaller than the critical value necessary for onset of instability for this $\hat{\sigma}$ ($\hat{r}_{crit} = 66.94$). The critical value of the parameter $\hat{r}$ corresponds to the unrealistic value of $T_v^e \approx -1889$ K.

To place the model into a region in parameter space where instability is possible, the parameter $\hat{r}$ has to be at least larger than 1. However, positive $\hat{r}$'s correspond to atmospheric vertical temeprature gradients that are close to or larger than the adiabatic lapse rate. This corresponds to an atmosphere that is neutral or unstable throughout the year, which contradicts both the observations [LHS$^+$79, SK77, MSS99] and the GCM simulations [PHSL90, HPB$^+$93].

Numerical simulations support the conclusion that the uncoupled model is in a stable regime. Figure 3.6 shows a 5 year run of the uncoupled LOM. The model parameters are the same as in Chapter 2. The upper panel shows zonal winds u_s (dashed) and u_a (solid). The middle panel shows the mean stream functions ψ_s (solid) and ψ_a (dashed). The lower panel shows temperatures T_{ns} (solid),$-T_v$ (dashed), T_{em} (dotted) and $c_4 T_{av}$ (dashed-dotted). It is clear that the behavior of the model is periodic in this case. Low frequency oscillations of the model variables are purely seasonal. Variations of the model parameters in the range appropriate for Mars do not produce aperiodic behavior in the uncoupled model.

The analysis of the Section 3.3 can be extended to the special case of a dusty atmosphere with uniform dust distribution. Assuming that atmospheric motions do not affect the dust distribution, the dust can be accounted for by decreasing the

radiative damping time t_r and the equilibrium vertical temperature parameter T_v^e, and increasing the equilibrium horizontal temperature parameter T_{ns}^e. The solutions of the uncoupled system will remain stable, since the control parameter $\hat{r}$ would still be much less than $\hat{r}_{crit}$. This circumstance may be used in the analysis of the decay phase of the GDS, when the dust source is no longer active and the dust distribution is more or less uniform.

Hence, it can be concluded that the behavior of the uncoupled LOM is stable for a clear atmosphere and for the atmosphere with a static uniform dust distribution. The behavior of the coupled LOM, however, can be expected to be more complex, since it includes the interactive surface dust source and dynamically redistributes radiatively active dust in the atmosphere. The behavior of the coupled LOM, as well as the LOM under the influence of stochastic forcing, will be considered in Part II.

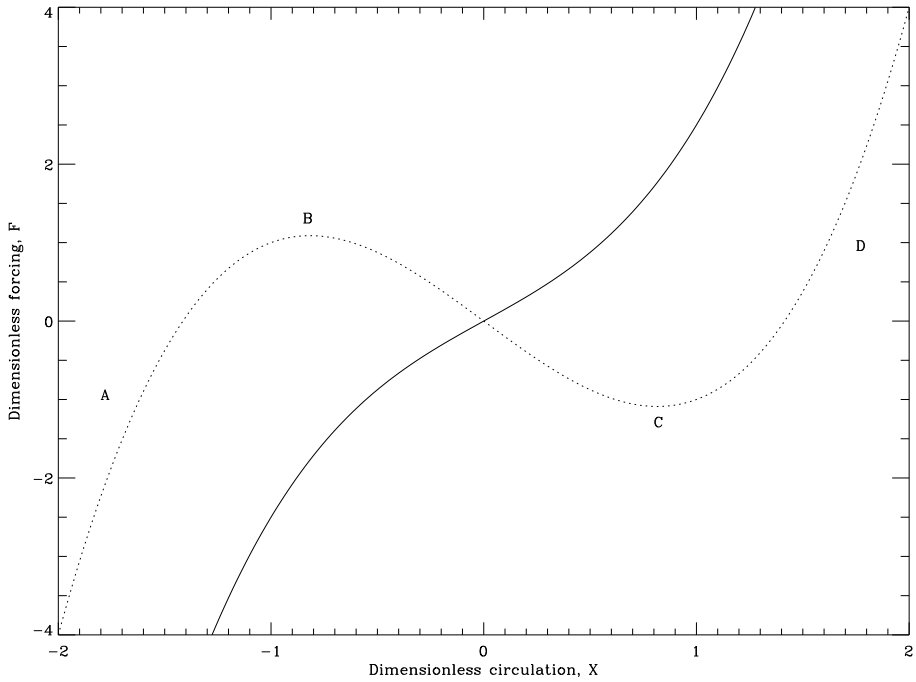

Figure 3.1: Schematic diagram illustrating the stability of solutions of the system (3.1)-(3.3) with constant forcing. The curves represent steady state solutions with constant forcing F for $\hat{r} = -0.5$ (solid curve) and for $\hat{r} = 3$ (dashed curve). Letters B and C indicate boundaries of the unstable region, while A and D denote stable regions on the dashed curve. For $\hat{r} \leq 1$ all solutions are stable. For $1 < \hat{r} \leq \hat{r}_{crit}$ solutions are unstable for $B < X < C$, and stable for $X \leq B$ and $X \geq C$. For $\hat{r} \geq \hat{r}_{crit}$ the system possesses aperiodic solutions. See text for details.

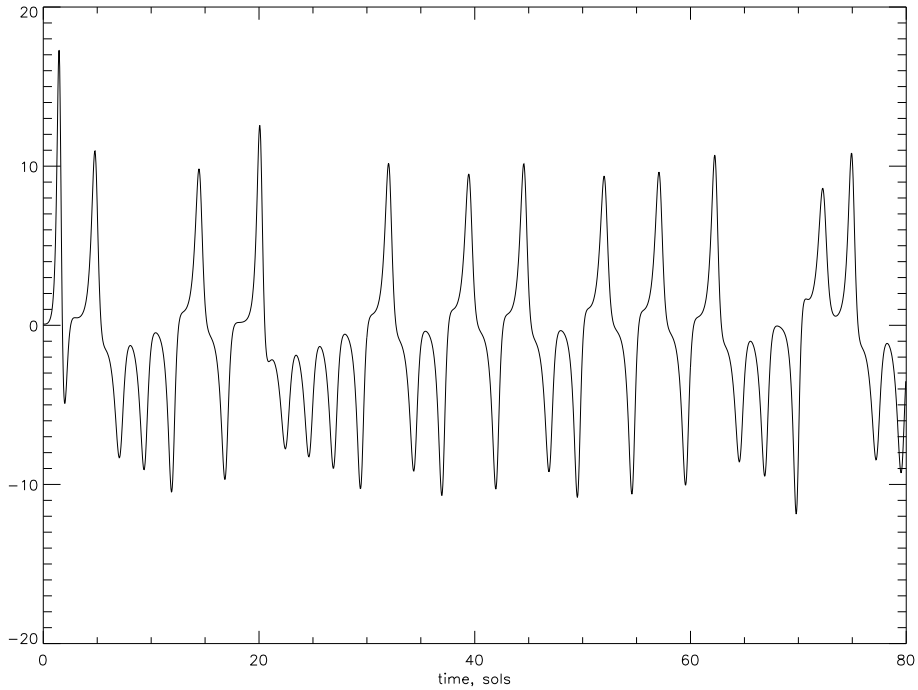

Figure 3.2: Time series of the model variable X for the first 80 sols of integration (2000 iterations). $\hat{\sigma} = 10$, $\hat{r} = 25$, $F = 0.9$.

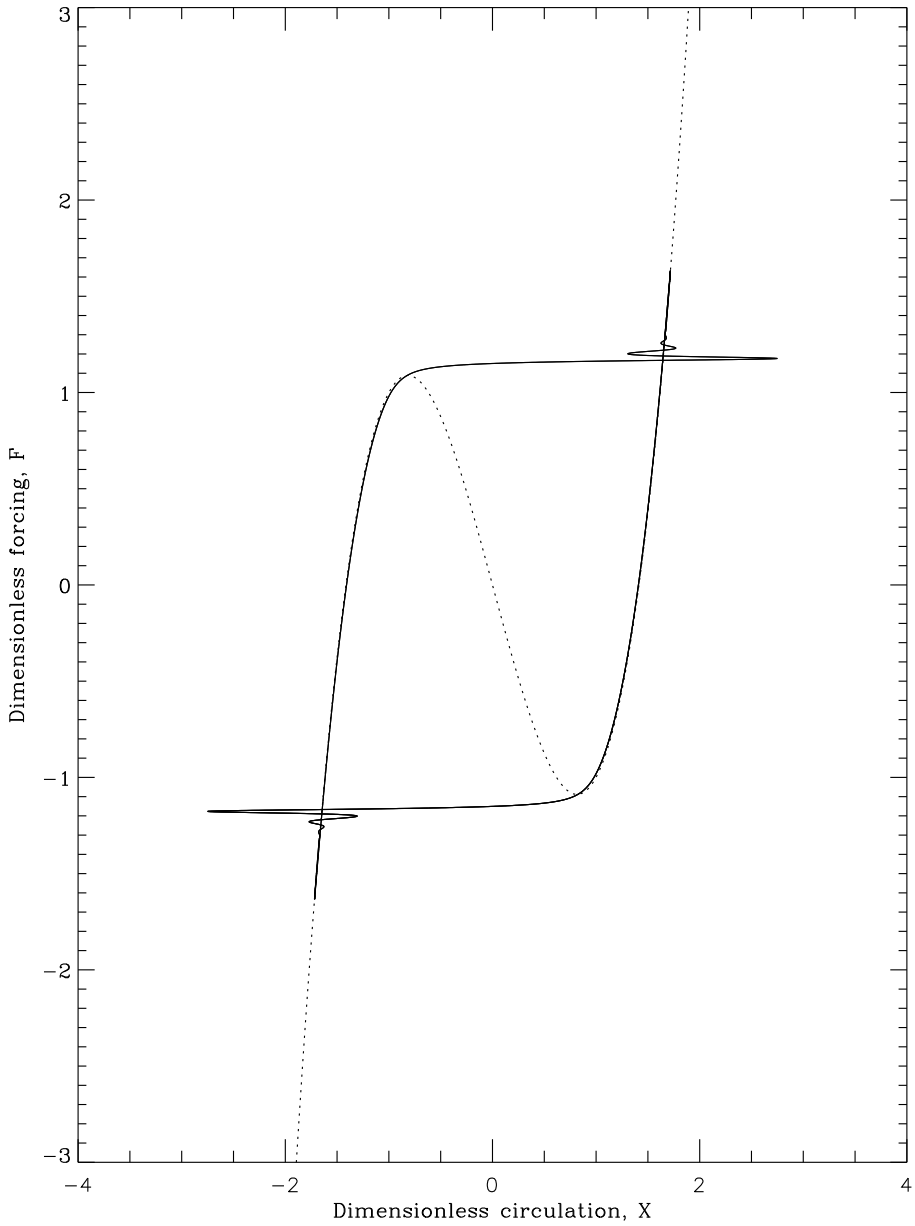

Figure 3.3: Behavior of the Lorenz system with periodic forcing for $1 < \hat{r} < \hat{r}_{crit}$. The dotted curve represents steady state solutions of the Eqs. (3.1)-(3.3) for $\hat{\sigma} = 65$, $\hat{r} = 3$. The solid curve represents trajectory of the state of the system in the (F, X) plane calculated for $F = 1.6$ and annual frequency.

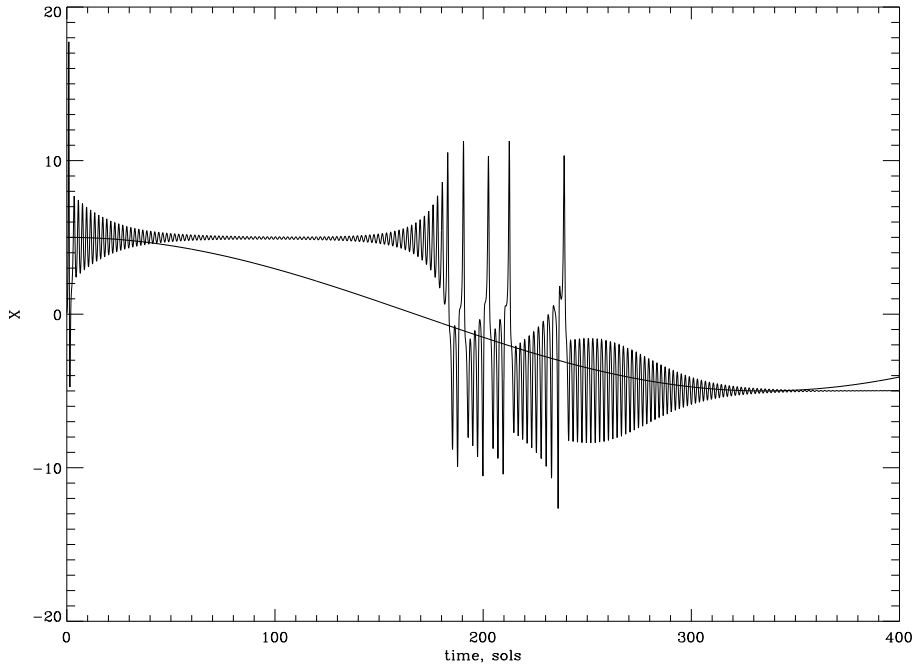

Figure 3.4: Time series of the model variable X for first 400 sols of integration (20000 iterations). $\hat{\sigma} = 10$, $\hat{r} = 25$, $F = 5$. The smooth curve is periodic forcing $F(t)$.

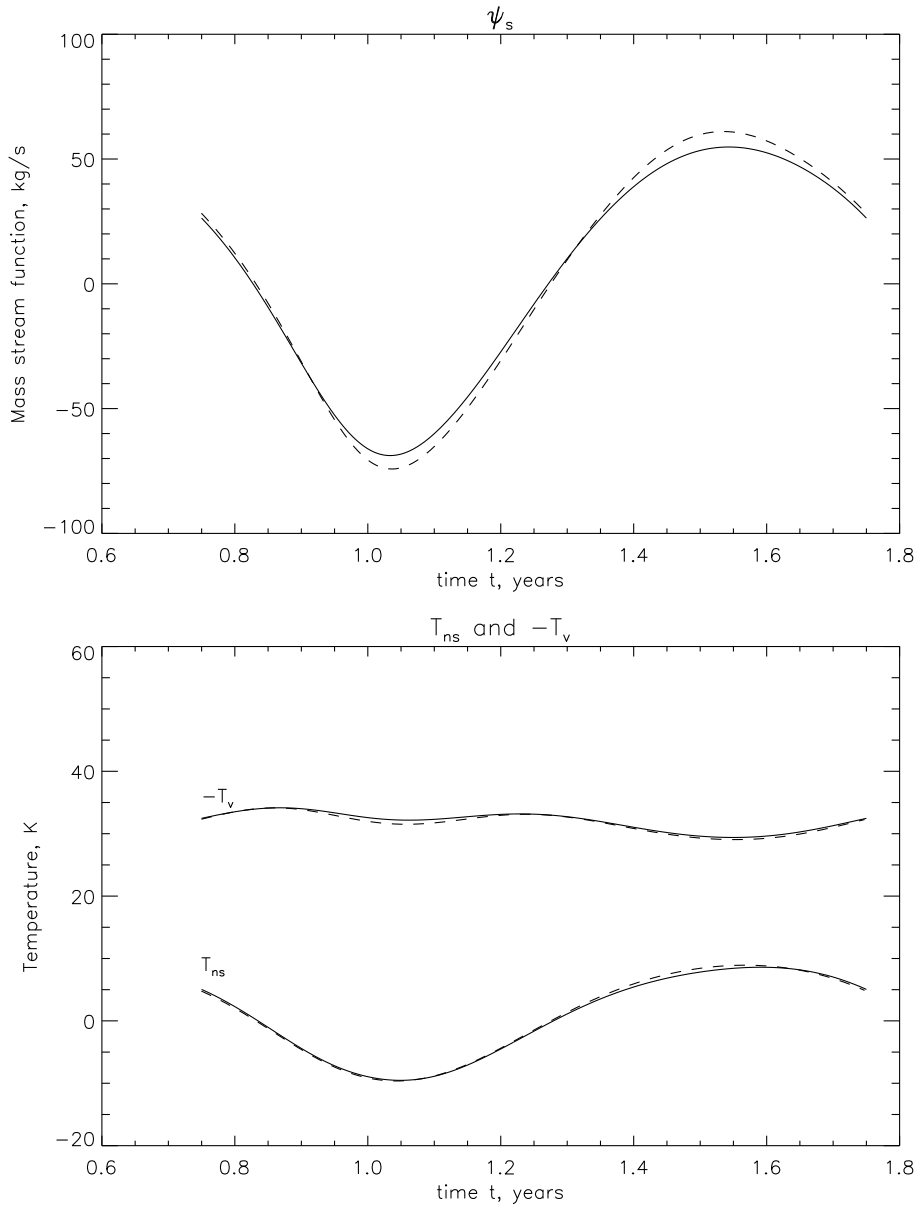

Figure 3.5: Comparison of the stream function ψ_s and temperatures T_{ns} and $-T_v$ calculated with the full LOM and using Eqs. (3.1)-(3.3). The upper panel shows the stream function ψ_s vs. time in units of 10^8 kg s^{-1} calculated for one martian year with the full LOM (solid line), and using analogy with the Lorenz system (dashed line). A year starts at perihelion ($L_s \approx 251°$). Negative values of ψ_s correspond to air rising in SH and positive values correspond to air rising in NH. The lower panel shows temperatures T_{ns} and $-T_v$ calculated for one martian year with the full LOM (solid line), and using analogy with the Lorenz system (dashed line). Negative values of T_{ns} correspond to warmer SH and visa versa.

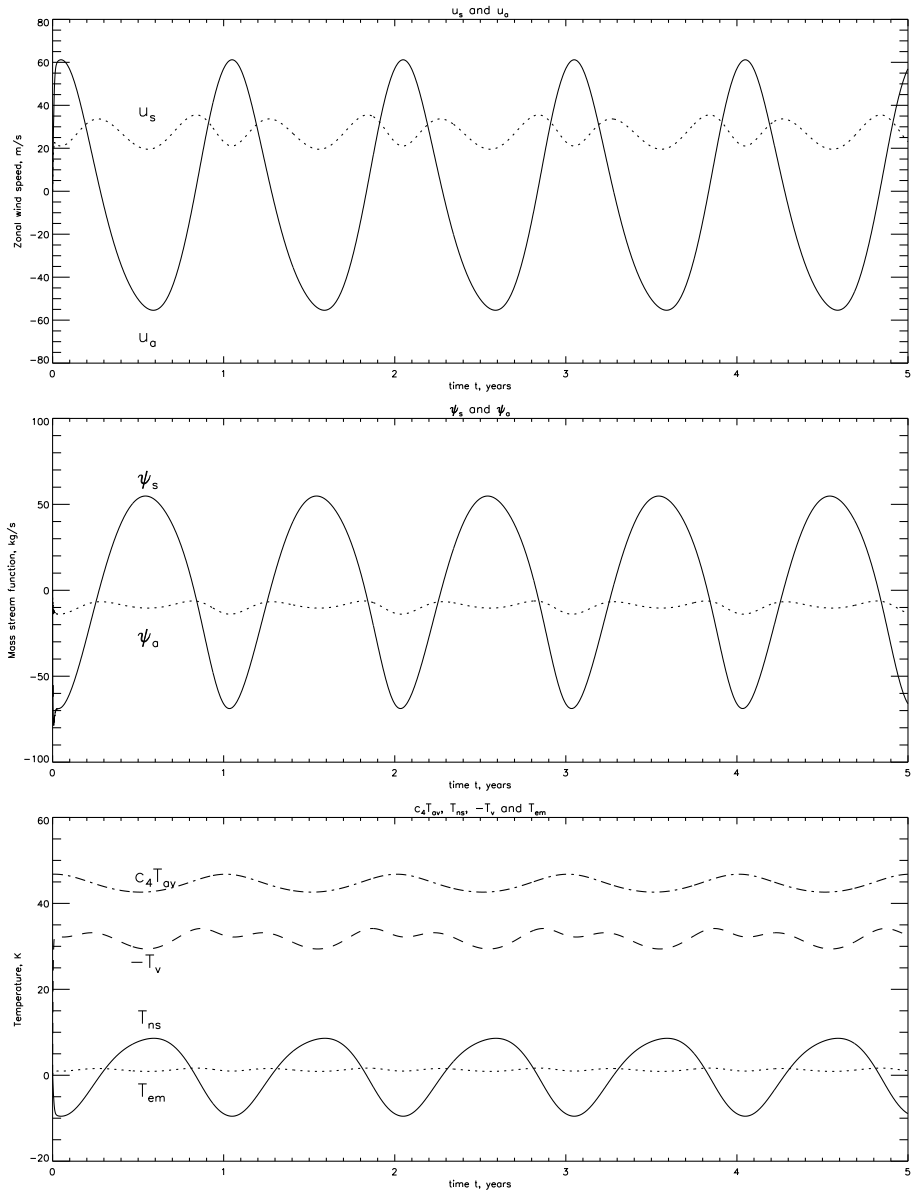

Figure 3.6: Time series of the LOM variables for the run without dust. Parameters of the model are the same as in Chapter 2.

Chapter 4 Conclusions

A simplified LOM of the martian global circulation was developed. The model is capable of simulating zonal mean circulation and dust transport in the Hadley cell. The model is constructed by Galerkin projection of the primitive equations onto the truncated set of basis functions. The basis functions and the parameter values are chosen based on the analysis of the results of the Ames GCM. The forcing of the model is described by simplified physics based on Newtonian cooling and Rayleigh friction. An interactive surface source of dust is included in the model. The dependence of the dust source on the surface winds is modeled after wind tunnel experiments. The LOM was validated by comparison to GCM simulations and observations.

By tuning the model parameters it was possible to reproduce very well the meteorological fields generated by the Ames GCM for all seasons and various dust loadings, except at southern winter solstice. However, by assuming that the frictional parameter r varies by a factor of 2 during the year, it was possible to reproduce the GCM results for all seasons with one set of model parameters. Variations in the friction parameter r can be attributed to seasonal changes in wave and eddy activity, or (and) to drastic topographic difference between NH and SH.

The LOM reproduces reasonably well the location and strength of the zonal jets, the strength, structure and width of the cross equatorial Hadley cell at solstice, of two weaker Hadley cells at equinox, and the structure of the temperature fields. Discrepancies can be attributed to the lower spatial resolution of the LOM, assumed flat topography, and simplified treatment of the effects of dust on atmospheric heating. Given the simplicity of the model the similarities are remarkable.

Experiments with interactive dust source compare very well with VL1 and VL2 observations of GDS. By tuning the threshold friction speed and amplitude of the source it was possible to reproduce closely the time of occurrence, intensity and duration of the second GDS of 1977. The first storm of 1977, which occurred before

perihelion, could not be reproduced by the LOM just by lowering the threshold friction speed. To reproduce two GDSs during southern summer, some kind of a negative feedback mechanism is needed to turn off the dust source shortly after the start of the first storm.

Finally, a subspace of the LOM parameter space was investigated analytically using analogy with the Lorenz system with periodic forcing. The analysis indicates that solutions of the LOM without dust transport or interactive source are stable in the parameter range suitable for Mars. Numerical experiments with the uncoupled LOM support this conclusion. The behavior of the coupled LOM, however, can be expected to be more complex, since it includes the interactive surface dust source and dynamically redistributes radiatively active dust in the atmosphere.

The LOM is suitable for conducting long term studies of the martian climate. The results of the model's application to the problem of interannual variability of GDS are reported in Part II of the thesis.